THE CMB ANISOTROPY EXPERIMENTS

Cosmic Microwave Background

GEORGE F. SMOOT
Lawrence Berkeley National Lab & Physics Department
University of California
Berkeley CA 94720

1. Abstract

Anisotropies in the cosmic microwave background (CMB) encode information about the evolution and development of the Universe. It is understood that quality observations of the CMB anisotropies can provide a very strong test of cosmological models and provide high precision measurements of major cosmological parameters. This paper provides a review of the COBE DMR results, the current status of the measurements of the CMB anisotropy power spectrum and then focuses on the programs that are likely to provide additional results including both suborbital observations and the two selected satellite missions: the NASA MIDEX mission MAP and the ESA M3 mission Max Planck Surveyor (formerly COBRAS/SAMBA). This review includes both a description of the experimental programs and the expected quality level of results.

2. Introduction

The observed cosmic microwave background (CMB) radiation provides strong evidence for the big bang model of cosmology and is the best probe we have for determining conditions in the early Universe as well as determining many important cosmological parameters. The angular power spectrum of the CMB contains information on virtually all cosmological parameters of interest, including the geometry of the Universe (Ω), the baryon density (Ω_B), the Hubble expansion rate (h), the cosmological constant (Λ), the number of light neutrinos (n_ν), the ionization history of the Universe, and the amplitudes and spectral indices of the primordial and tensor perturbation spectra. Precise CMB observations, data analysis, and interpretation can distinguish between cosmological models. They can be used to verify that the range of models under consideration is plausible and to distinguish between models with primordial perturbations (e.g. the inflationary big bang) or those with active perturbations (e.g. topological defects which must result from spontaneous symmetry breaking of unified forces). Once a model is thus singled out, its parameters can, in principle, be determined to accuracies of the order of a per cent[38].

Since the initial detection of CMB temperature anisotropies by the *COBE* DMR [71], over a dozen other balloon-borne and ground-based experiments have reported anisotropy detections on smaller angular scales. With the existence of anisotropies now firmly established, observational goals have shifted towards an accurate determination of the CMB anisotropy power spectrum over a wide range of angular scales. The reasons for this are two-fold. (1) If the processes producing the initial fluctuations are stochastic and random phase, then the power spectrum contains all the information of the underlying physical model. (2) It is observationally easier to obtain a power spectrum than a fully reliable map. Several technical advances, including improved receivers, interferometry, and long-duration balloon flights, hold great promise for high-precision maps in the next few years. Ultimately, the two approved satellites: NASA MidEX mission MAP and ESA M3 mission Planck are expected to provide high-angular-resolution high-sensitivity maps of the entire sky in multifrequency bands. Thus we can anticipate increasingly complex data sets requiring sophisticated analysis: COBE DMR 4-year maps (6144 pixels), the CfPA balloon experiments MAXIMA/BOOMERANG (26,000 to 130,000 pixels), MAP ($\approx$400,000 pixels), and Planck ($> 10^6$ pixels). These maps then hold the promise of revolutionizing cosmology in terms of making it significantly more precise in quantitative terms.

It is the goal of these lectures to provide the background necessary to understand the existing data, soon to be achieved data from experiments in progress, and finally the forthcoming data from the more advanced experiments and space missions. We proceed with some historical context, a review of the COBE observations both for the discovery of anisotropy and as a prototype for the next generation of space missions, a review of the current and proposed generations of balloon-borne experiments and interferometers, and finally a discussion of the new space-based experiments.

3. CMB Background

Primordial nucleosynthesis calculations require a cosmic background radiation (CBR) with a temperature $kT \sim 1$ MeV at a redshift of $z \sim 10^9$. Gamow, Alpher, & Herman [3] realized that this CBR was required and predicted its evolution to a faint residual relic radiation with a current temperature of a few degrees. Our more modern view of the hot big bang models gives the cosmic background radiation a very central role in the development of the Universe.

The CMB was serendipitously discovered by Penzias & Wilson [62] in 1964 (published in 1965) and they noted that it was isotropic to the sensitivity of their measurement ($< 10\%$). The observed CMB spectrum is well characterized by a 2.73 ± 0.01 K blackbody spectrum. The hot big bang model predicts that the CBR should have a thermal spectrum and this is verified precisely. Combined with the observed spectrum of the dipole anisotropy, this precision thermal spectrum also provides us with the knowledge and ability to separate CMB anisotropies from the various foregrounds. Anisotropies will in general have a spectrum set by the derivative of the CMB spectrum. See my previous lectures for a more complete discussion of the expected anisotropy spectrum.

4. Theoretical Anisotropies

There are three primary threads of science that are pursued by CMB anisotropy measurements:

(1) Initial Conditions for Large Scale Structure Formation: The formation of galaxies, clusters of galaxies, and large scale structures is a key issue in cosmology. Theory indicates that whatever the seeds of structure formation, they will leave their imprint as anisotropies in the CMB. Different scenarios for structure formation will leave different anisotropies.

(2) Physics of the Early Universe: CMB anisotropy measurements are a probe of the ultra-high energy physics and processes that occur in the very early universe. These observations are a probe of inflation or quantum gravity and a test of potential topological defects (monopoles, strings, domain walls, and textures) that must result from spontaneous symmetry breaking.

(3) Geometry and Dynamics of the Universe: Observations of the CMB anisotropies provide information on the metric and topology of the space-time, the isotropy of expansion of space-time, the curvature of space, and the possible rotation and shear of the Universe.

There is now a fairly extensive literature on the first two areas and the third is what we consider classical cosmology. In the early history of the field all measurements led only to upper limits on CMB anisotropy and these in turn led to limits on but not a measurement of these processes.

A major finding of the initial *COBE* DMR discovery [71] was that the CMB was anisotropic on all observed angular scales. A key question is what these anisotropies represent. Immediately, the interpretation focused upon the seeds of large scale structure formation. In the early 1970's the observed large scale structure and scaling arguments led to the prediction [60],[31],[85] that the primordial gravitational potential perturbations must have an equal *rms* amplitude on all scales. This corresponds to a matter density perturbation power-law spectrum, $P(k) \propto k^n$, where k is the comoving wavenumber, with $n = 1$. At that time there were no known mechanisms for producing such a scale-invariant power spectrum of fluctuations. In 1982 it was found that inflationary models predicted nearly scale-invariant perturbations as a result of quantum mechanical fluctuations at very early times. Even with the proliferation of inflationary models, it is found that essentially all reasonable inflationary models predict $n \approx 1$. Presumably, a more reasonable class of inflationary models will result in requiring a tie to particle physics. It is now known that topological defects naturally produce scale-invariant fluctuations. Thus there are at least two known mechanisms for producing a nearly scale invariant primordial perturbation spectrum.

The translation from a scale-invariant spectrum of perturbations to the CMB temperature anisotropies depends upon angular scale and the contents of the universe. On large angular scales the results of most models are fairly similar. Including the effects of a standard cold dark matter model, a Harrison-Zeldovich $n = 1$ universe is consistent with the power spectrum measured by the *COBE* DMR data. The observed power spectrum of fluctuation amplitudes is also consistent with models of large scale structure formation based upon primordial seeds produced by quantum fluctuations or topological defects in the early universe.

The physics of anisotropy caused by primordial density perturbations is usually divided into four generic areas although they are all treated properly in the full Sachs-Wolfe effect [67]. These effects are: the gravitational redshift which dominates at large angular scales, the (Rees-Sciama) effect on light propagating through a changing potential, the Doppler effect caused by the motion of the observer or the source, and temperature or entropy variations.

Models of the formation of structure in the Universe fall into two broad classes: inflationary and defect models. Each model predicts an angular power spectrum of CMB anisotropy described in terms of the amplitude of the spherical harmonic of multipole order ℓ.

The most detailed theoretical work has been carried out for inflationary models. Hu and White [37] have argued that all inflationary models produce an angular power spectrum with a unique set of "doppler" or "acoustic" peaks between $\ell = 100$ and $\ell = 1000$ ($11' < \theta < 1.8°$). The relative position and height and the detailed shape of the peaks provides more independent constraints than there are parameters in the inflationary scenario and allow their determination.

Defect models, including cosmic strings and textures, provide an alternative to inflation. Such models predict a non-gaussian distribution of temperature fluctuations and a power spectrum different from that of inflation.

Most cosmological models do not predict the exact CMB temperature pattern that would be observed in our sky, but rather predict a statistical distribution of anisotropies. In the context of such models, the CMB temperature observed in our sky is only a single realization drawn from the cosmic statistical distribution. Theoretical models most often predict a power spectrum in spherical harmonic amplitudes; as the physics of the models leads to primordial fluctuations that are Gaussian random fields, the power spectrum is sufficient to characterize the results. Observations of the sky can be expressed as a spherical harmonic temperature expansion $T(\theta,\phi) = \sum_{\ell m} a_{\ell m} Y_{\ell m}(\theta,\phi)$. If the original perturbations are Gaussian random fields, the $a_{\ell m}$ are Gaussianly distributed, and the power at each ℓ is $(2\ell+1)C_\ell/(4\pi)$, where $C_\ell \equiv \langle |a_{\ell m}|^2 \rangle$, is sufficient to characterize the results. For an idealized full-sky observation, the variance of each measured C_ℓ is $[2/(2\ell+1)]C_\ell^2$. This sampling variance (known as cosmic variance) comes about because each C_ℓ is chi-squared distributed with $(2\ell+1)$ degrees of freedom for our observable volume of the Universe [80]. Thus, in addition to experimental uncertainties, we account for the *cosmic sample variance* uncertainties due to our observation of a single realization in our analyses of the DMR maps. Cosmic variance exists independently of the quality of the experiment. The power spectrum from the 4-year DMR map is cosmic variance limited for $\ell \lesssim 20$.

5. The Legacy of COBE

The Cosmic Background Explorer (*COBE*) was NASA's first satellite dedicated to cosmology and is a milestone for that and for the legacy of information that it has provided on the early Universe. Much of its results are from observations of the cosmic microwave background (CMB). The CMB is a pillar of the Big Bang model and encodes information about energy release in the early Universe, primordial perturbations, and the geometry of the universe. As mentioned previously the CMB contains information on critical cosmological parameters such as Ω_0, Ω_B, Ω_Λ, and H_0. *COBE's* legacy of the precise measurement of the CMB spectrum and the discovery and early mapping of the CMB anisotropy low-ℓ power spectrum provides a position from which to carry out a program testing our cosmological theories and understanding the early Universe precisely.

The Differential Microwave Radiometers (DMR) experiment ([70]) discovered CMB anisotropies from analysis of its first year of data [71], [9], [82], [41]. The CMB temperature fluctuations were measured at an angular resolution of 7° at frequencies of 31.5, 53, and 90 GHz. These results were supported by a detailed examination of the DMR calibration and its uncertainties ([10]) and a detailed treatment of the upper limits on residual systematic errors ([41]). The *COBE* results were confirmed by the positive cross-correlation between the *COBE* data and data from balloon-borne observations at a shorter wavelength [29] and later by comparison of the *COBE* data and data from the ground-based Tenerife experiment [49] at longer wavelengths. The positive correlation at both longer and shorter wavelengths provides confidence in the results. The results from analysis of two years of DMR data [7] reconfirmed the results from the first year data.

This section summarizes the key and most recent results from COBE. Details can be found in the original references and in the most recent FIRAS paper [28] and in a set of DMR 4-year analysis papers [4], [5], [6], [30], [33], [34], [50], [43], [44], [45], [83].

5.1. THE *COBE* DMR INSTRUMENTS & DATA ANALYSIS

The DMR consists of 6 differential microwave radiometers: 2 nearly independent channels, labeled A and B, at frequencies 31.5, 53, and 90 GHz (wavelength 9.5, 5.7, and 3.3 mm respectively). Each radiometer measures the difference in power between two 7° fields of view separated by 60°, 30° to either side of the spacecraft spin axis [70]. Figure 1 shows a schematic signal path for the DMRs. *COBE* was launched from Vandenberg Air Force Base on 18 November 1989 into a 900 km, 99° inclination circular orbit, which precesses to follow the terminator (light dark line on the Earth) as the Earth orbits the Sun. Attitude control keeps the spacecraft pointed away from the Earth and nearly perpendicular to the Sun with a slight backward tilt so that solar radiation never directly illuminates the aperture plane. The combined motions of the spacecraft spin (75 s period), orbit (103 m period), and orbital precession ($\sim 1°$ per day) allow each sky position to be compared to all others through a highly redundant set of temperature difference measurements spaced 60° apart. The on-board processor box-car integrates the differential signal from each channel for 0.5 s, and records the digitized differences for daily playback to a ground station.

Ground data processing consists of calibration, extensive systematic error analyses, and conversion of time-ordered-data to sky maps [43]. Checks on the correlated noise in the maps [48] due to the map-making process indicate they are well below the 1% level. The DMR time-ordered-data include systematic effects such as emission from the Earth and Moon, the instrument's response to thermal changes, and the instrument's response to the Earth's magnetic field. The largest detected effects do not contribute significantly to the DMR maps; they are either on time scales long compared to

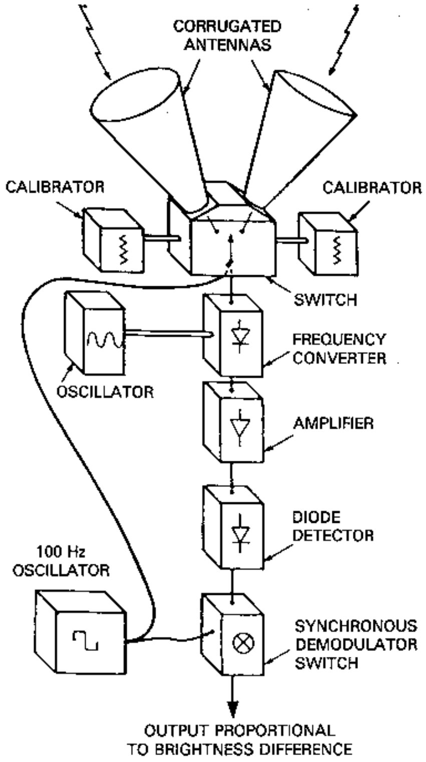

Figure 1. DMR signal flow schematic

the spacecraft spin sampling (e.g. thermal gain drifts) or have time dependence inconsistent with emission fixed on the celestial sphere (e.g. magnetic effects). Detected and potential systematic effects were quantitatively analyzed in detail [43]. Data with the worst systematic contamination (lunar emission, terrestrial emission, and thermal gain changes) were not used in the map-making process and constitute less than 10% of the data in the 53 and 90 GHz channels. The remaining data were corrected using models of each effect. The data editing and correction parameters were conservatively chosen so that systematic artifacts, after correction, are less than 6 μK rms (95% confidence upper limit) in the final DMR map in the worst channel. This is significantly less than the levels of the noise and celestial signals.

A dipole $T_d = 3.356$ mK anisotropy signal (thermodynamic temperature in Galactic coordinates Cartesian components [X,Y,Z] = [-0.2173, -2.2451, +2.4853] mK) is subtracted from the time-ordered differential data prior to forming the 4-year sky maps to reduce spatial gradients within a single pixel. A small residual dipole remains in the maps from a combination of CMB and Galactic emission. The mean signal-to-noise ratios in the 10°

smoothed maps are approximately 0.5, 1.5, and 1.0 for 31, 53, and 90 GHz, respectively. For a multi-frequency co-added map the signal-to-noise ratio is ~ 2. This signal-to-noise level is adequate to portray an accurate overall visual impression of the anisotropy. Visual comparison of the full sky maps at each frequency, after averaging the A and B channels, removing the CMB dipole, and smoothing to $10°$ effective resolution show coincident features. Well off the Galactic plane these are clearly true CMB anisotropy features. Simulated data in combination with the noise appropriate to 1-, 2-, and 4-years of DMR 53 GHz observations show the convergence of the DMR maps with the input simulated data. Increasing years of data result in the emergence of the input large scale features. We can be confident that the large scale features in the 4-year DMR maps are real features rather than confusing noise.

Given the sensitivity of the 4-year DMR maps we have extended the cut made in our previous analyses to exclude additional Galactic emission. We use the *COBE* DIRBE 140 μm map as a guide to cut additional Galactic emission features. The full sky DMR maps contain 6144 pixels. An optimum Galactic cut maximizes the number of remaining pixels while minimizing the Galactic contamination. This cut leaves 3881 pixels (in Galactic pixelization) while eliminating the strongest $|b| > 20°$ Galactic emission. Moderate changes to this cut will cause derived CMB parameters to change somewhat, but this is consistent with the data sampling differences of real CMB anisotropy features and not necessarily Galactic contamination. Likewise, derived CMB parameters also vary by the expected amount when the maps are made in ecliptic rather than Galactic coordinates since about 1/2 of the noise is re-binned.

Kogut et al. [44] examine the Galactic contamination of the high Galactic latitude regions of the DMR maps which remain after the Galactic emission cut (described above). No significant cross-correlation is found between the DMR maps and either the 408 MHz synchrotron map or the synchrotron map derived from a magnetic field model [9]. This places an upper limit $T_{\rm synch} < 11$ μK (95% confidence) on synchrotron emission at 31 GHz.

A significant correlation is found between the DMR maps and the dust-dominated DIRBE 140 μm map, with frequency dependence consistent with a superposition of dust and free-free emission. The correlation is really with a component of Galatic emission with a spectral index of about -2.1 which could be very flat spectrum synchrotron as expected where cosmic ray electron acceleration is actually occuring. We use the term free-free to stand for this component which corresponds to a $7°$ rms free-free emission component of 7.1 ± 1.7 μK at 53 GHz and a dust component of 2.7 ± 1.3 μK at 53 GHz. Since this emission is uncorrelated with CMB anisotropies it constitutes $< 10\%$ of the CMB power. The amplitude of the correlated free-free component at 53 GHz agrees with a noisier estimate of free-free emission derived from a linear combination of DMR data which includes *all* emission with free-free spectral dependence. The combined dust and free-free emission contribute 10 ± 4 μK *rms* at both 53 and 90 GHz, well below the 30 μK cosmic signal. These Galactic signal analyses are consistent with the fact that the fitted cosmological parameters are nearly unaffected by removal of modeled Galactic signals [30], [33] with the notable exception of the quadrupole, which has significant Galactic contamination [44]. A search by Banday et al. [4] finds no evidence for significant extragalactic contamination of the DMR maps.

5.2. FOUR-YEAR DMR RESULTS

Monopole $\ell = 0$: Despite the fact that the DMR is a differential instrument, the known motion of the *COBE* spacecraft about the Earth and the motion of the Earth about the Solar System barycenter provides a means to determine the CMB monopole temperature from the DMR data. The CMB at millimeter wavelengths is well described by a blackbody spectrum [54],[28]. The Doppler effect from the combined spacecraft and Earth orbital motions creates a dipole signal $T(\theta) = T_0[1 + \beta\cos(\theta) + O(\beta^2)]$, where $\beta = v/c$ and θ is the angle relative to the time-dependent velocity vector. The satellite and Earth orbital motions are well known and change in a regular fashion, allowing their Doppler signal to be separated from fixed celestial signals. We fit the time-ordered data to the Doppler dipole and recover a value for the CMB monopole temperature, $T_0 = 2.725 \pm 0.020$ K [43].

Dipole $\ell = 1$: The CMB anisotropy is dominated by a dipole term attributed to the motion of the Solar System with respect to the CMB rest frame. A precise determination of the dipole must account for Galactic emission and the aliasing of power from higher multipole orders once pixels near the Galactic plane are discarded. One can account for Galactic emission by using a linear combination of the DMR maps or by cross-correlating the DMR maps with template sky maps dominated by Galactic emission [44]. The high-latitude portion of the sky is fitted for a dipole with a CMB frequency spectrum using a pixel-based likelihood analysis [33]. Accounting for the smoothing by the DMR beam and map pixelization, the CMB dipole has amplitude 3.353 ± 0.024 mK toward Galactic coordinates $(l, b) = (264°.26 \pm 0°.33, 48°.22 \pm 0°.13)$, or equatorial coordinates $(\alpha, \delta) = (11^{\rm h}12^{\rm m}2 \pm 0^{\rm m}8, -7°.06 \pm 0°.16)$ epoch J2000.

A second analysis approach utilizes a phenomenological estimate of the Galactic foreground by examining the dipole fitted parameters as a function of cuts in Galactic latitude. It was found that the largest source of error in the dipole direction was reduced by using lower Galactic latitude cuts. Using the four year data set from all six channels of the COBE Differential Microwave Radiometers (DMR), the best-fit dipole amplitude $3.358 \pm 0.001 \pm 0.023$ mK amplitude in the direction $(\ell, b) = (264^\circ.31 \pm 0^\circ.04 \pm 0^\circ.16, +48^\circ.05 \pm 0^\circ.02 \pm 0^\circ.09)$ where the first uncertainties are statistical and the second are estimates of the combined systematics [50].

These dipole measurements are consistent with previous DMR and FIRAS results.

Quadrupole $\ell = 2$: On the largest angular scales (e.g., quadrupole), Galactic emission is comparable in amplitude to the anisotropy in the CMB. The quadrupole amplitude is found by a likelihood analysis which simultaneously fits the high-latitude portion of the DMR maps for Galactic emission traced by synchrotron- and dust-dominated surveys and a quadrupole anisotropy with a thermodynamic frequency spectrum [44],[33]. After correcting for the positive bias from instrument noise and aliasing, the CMB quadrupole amplitude observed at high latitude is $Q_{rms} = 10.7 \pm 3.6 \pm 7.1$ μK, where the quoted errors reflect the 68% confidence uncertainties from random statistical errors and Galactic modeling errors, respectively. The observed quadrupole amplitude, Q_{rms}, has a lower value than the quadrupole expected from a fit to the entire power spectrum, Q_{rms-PS}, but whether this is a chance result of cosmic variance or reflects the cosmology of the Universe cannot be determined from *COBE* data. The 68% confidence interval for the quadrupole amplitude, 6 μK $\leq Q_{rms} \leq$ 17 μK, is consistent with the quadrupole normalization of the full power spectrum power-law fit (discussed below): $Q_{rms-PS} = 15.3^{+3.8}_{-2.8}$ μK.

Power spectrum $\ell \geq 2$: The simplest probe of the angular power spectrum of the anisotropy is its Legendre transform, the 2-point correlation function. The 2-point correlation function of the 4-year maps is analyzed by Hinshaw et al. [34], where it is shown that the 2-point data are consistent from channel to channel and frequency to frequency. The data are robust with respect to the angular power spectrum. A Monte Carlo-based Gaussian likelihood analysis determines the most-likely quadrupole normalization for a scale-invariant $(n = 1)$ power-law spectrum. The results are summarized in Table 1 which also includes the results of 3 additional, independent power spectrum analyses, discussed below. The normalization inferred from the 2-point function is now in better agreement with other determinations than was the case with the 2-year data. The change is due to data selection: with the 2-year data, we only analyzed the 53×90 GHz cross-correlation function; with the 4-year data we have analyzed many more data combinations, including the auto-correlation of a co-added, multi-frequency map. This latter combination is more comparable to the data analyzed by other methods, and the 2-point analysis yields consistent results in that case. The combined 31, 53 and 90 GHz CMB rms is 29±1 μK in the 10° smoothed map [5], consistent with the level determined by the 2-point results.

It is also possible to analyze the power spectrum directly in terms of spherical harmonics. However, there is considerable subtlety in this because the removal of the Galactic plane renders the harmonics non-orthonormal, producing strong correlations among the fitted amplitudes. Wright et al. [83] has solved for an angular power spectrum by modifying and applying the technique described by Peebles [59] and Hauser & Peebles [32] for data on the cut sphere. They compute a Gaussian likelihood on these data and calibrate their results with Monte Carlo simulations. Górski et al. [30] explicitly construct orthonormal functions on the cut sphere and decompose the anisotropy data with respect to these modes. They form and evaluate an exact Gaussian likelihood directly in terms of this mode decomposition. The results of these analyses are summarized in Table 1. Further details, including results from other data combinations are given in the respective papers.

Hinshaw et al. [33] evaluate a Gaussian likelihood directly in terms of a full pixel-pixel covariance matrix, a technique applied to the 2-year data by Tegmark & Bunn [76]. The results of the power-law spectrum fits are summarized in Table 1. Hinshaw et al. [33] also analyze the quadrupole anisotropy separately from the higher-order modes, to complement the analysis of Kogut et al. [44]. They compute a likelihood for the observed quadrupole Q_{rms}, nearly independent of higher-order power, and show that it peaks between 6 and 10 μK, depending on Galactic model, but that its distribution is so wide that it is easily consistent with the $Q_{rms-Ps} = 15.3^{+3.8}_{-2.8}\mu$K, the value derived using the full power spectrum.

An important lesson from fitting with different cuts and configurations and from our Monte Carlo simulations is that the best fitted parameters depend both upon the random statistics of CMB fluctuations and on the choice of cuts and fitting parameters. Table 1 in Gorski et al.[30] is indicative of the range of results obtainable using a robust and stable approach.

Tests for Gaussian Statistics: It is important to determine whether the primordial fluctuations are Gaussian. The probability distribution of temperature residuals should be close to Gaussian if the sky variance is Gaussian and the receiver noise is Gaussian. The receiver noise varies somewhat from pixel to pixel because the observation times are not all the same, but when this is taken into account the data appear Gaussian [72]. There is no evidence for an excess of large deviations, as would be expected if there were an unknown population of point sources. A search for point sources in the 2-year maps found none [42]. Given the large beam of the instrument and the variance of both cosmic signals and receiver noise, it is still possible for interesting signals to be hidden in the data.

Kogut et al. [45] compare the 4-year DMR maps to Monte Carlo simulations of Gaussian power-law CMB anisotropy. The 3-point correlation function, the 2-point correlation of temperature extrema, and the topological genus are all in excellent agreement with the hypothesis that the CMB anisotropy on angular scales of $7°$ or larger represents a random-phase Gaussian field. A likelihood comparison of the DMR maps against non-Gaussian χ^2_N toy models tests the alternate hypothesis that the CMB is a random realization of a field whose spherical harmonic coefficients $a_{\ell m}$ are drawn from a χ^2 distribution with N degrees of freedom. Not only do Gaussian power-law models provide an adequate description of the large-scale CMB anisotropy, but non-Gaussian models with $1 < N < 60$ are five times less likely to describe the true statistical distribution than the exact Gaussian model.

5.3. SUMMARY OF 4-YEAR *COBE* DMR CMB MEASUREMENTS

(1) The full 4-year set of *COBE* DMR observations is analyzed and full sky maps have been produced [6]. The typical signal-to-noise ratio in a $10°$ smoothed frequency-averaged map is ~ 2, enough to provide a visual impression of the anisotropy.

(2) The DMR (despite its being a differential instrument) finds a CMB monopole temperature of $T_0 = 2.725 \pm 0.020$ K [43]. This is in excellent agreement with the *COBE* FIRAS precision measurement of the spectrum of the CMB, $T_0 = 2.728 \pm 0.002$ K [28].

(3) The CMB dipole from DMR has amplitude 3.358 ± 0.024 mK toward Galactic coordinates $(l, b) = (264°.31 \pm 0°.16, 48°.05 \pm 0°.10)$, or equatorial coordinates $(\alpha, \delta) = (11^{\rm h}12^{\rm m}2 \pm 0^{\rm m}8, -7°.06 \pm 0°.16)$ epoch J2000. This is consistent with the dipole amplitude and direction derived by *COBE* FIRAS [28].

(4) The 95% confidence interval for the observed $\ell = 2$ quadrupole amplitude is $4\ \mu\mathrm{K} \le Q_{rms} \le 28\ \mu\mathrm{K}$. This is consistent with the value predicted by a power-law fit to the power spectrum yields a quadrupole normalization of: $Q_{rms-PS} = 15.3^{+3.8}_{-2.8}\ \mu$K [44]; [33].

(5) The power spectrum of large angular scale CMB measurements is consistent with an $n = 1$ power-law [30], [33], [83]. If the effects of a standard cold dark matter model are included, *COBE* DMR should find $n_{eff} \approx 1.1$ for a $n = 1$ universe. With full use of the multi-frequency 4-year DMR data, including our estimate of the effects of Galactic emission, we find a power-law spectral index of $n = 1.2 \pm 0.3$ and a quadrupole normalization $Q_{rms-PS} = 15.3^{+3.8}_{-2.8}\ \mu$K. For $n = 1$ the best-fit normalization is $Q_{rms-PS}|_{n=1} = 18 \pm 1.6\ \mu$K. Differences in the derived values of Q and n between various analyses of DMR data are much more dependent on the

Technique	n [a]	Q_{rms-PS} [b] (μK)	$Q_{rms-PS\|n=1}$ [c] (μK)
No Galaxy Correction [d]			
2-point correlation function [34]	—	—	$17.5^{+1.4}_{-1.4}$
Orthogonal functions [30]	$1.21^{+0.24}_{-0.28}$	$15.2^{+3.7}_{-2.6}$	$17.7^{+1.3}_{-1.2}$
Pixel temperatures [33]	$1.23^{+0.26}_{-0.27}$	$15.2^{+3.6}_{-2.8}$	$17.8^{+1.3}_{-1.3}$
Hauser-Peebles cut sky [83]	—	—	—
Internal Combination Galaxy Correction [e]			
2-point correlation function [34]	—	—	$16.7^{+2.0}_{-2.0}$
Orthogonal functions [30]	$1.11^{+0.38}_{-0.42}$	$16.3^{+5.2}_{-3.7}$	$17.4^{+1.8}_{-1.7}$
Pixel temperatures [33]	$1.00^{+0.40}_{-0.43}$	$17.2^{+5.6}_{-4.0}$	$17.2^{+1.9}_{-1.7}$
Hauser-Peebles cut sky [83]	$1.62^{+0.44}_{-0.50}$	—	$19.6^{+2.5}_{-2.5}$

[a]Mode & 68% confidence range of the projection of the 2-d likelihood, $L(Q,n)$, on n
[b]Mode & 68% confidence range of the projection of the 2-d likelihood, $L(Q,n)$, on Q
[c]Mode & 68% confidence range of the slice of the 2-d likelihood, $L(Q,n)$, at $n=1$
[d]Formed from the weighted average of all 6 channels
[e]from a linear combination of 6 channel maps canceling free-free emission [44]

TABLE 1. Summary of DMR 4-Year Power Spectrum Fitting Results.

detailed data selection effects than on the analysis technique.

(6) The DMR anisotropy data are consistent with Gaussian statistics. Statistical tests prefer Gaussian over other toy statistical models by a factor of ~ 5 [45].

5.4. COBE CONCLUSIONS

The COBE-discovered [71] higher-order ($\ell \geq 2$) anisotropy is interpreted as being the result of perturbations in the energy density of the early Universe, manifesting themselves at the epoch of the CMB's last scattering. These pertubations are the seeds of large scale structure formation and are relics from processes occurring in the very early Universe at extremely high energies. In the standard scenario the last scattering of cosmic background photons takes place at a redshift of approximately 1100, at which epoch the large number of photons was no longer able to keep the hydrogen sufficiently ionized. The optical thickness of the cosmic photosphere is roughly $\Delta z \sim 100$ or about 10 arcminutes, so that features smaller than this size are damped. Observations of the CMB anisotropy power spectrum can reveal to us much of the interesting history of the early Universe and so a great deal of effort has gone into its observation.

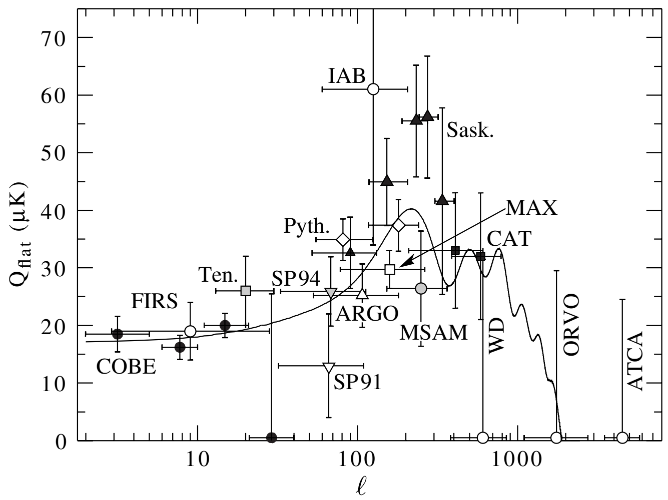

Figure 2. Current status of CMB anisotropy observations: Plotted are the quadrupole amplitudes for a flat (unprocessed scale-invariant spectrum of primordial perturbations, i.e., a horizontal line) anisotropy spectrum that would give the observed results for the experiment. The vertical error bars represent estimates of 68% CL, while the upper limits are at 95% CL. Horizontal bars indicate the range of ℓ values sampled. The curve indicates the expected spectrum for a standard CDM model ($\Omega_0 = 1$, $\Omega_B = 0.05$, $h = 0.5$), although true comparison with models should involve convolution of this curve with each experimental filter function.

6. Current Anisotropy Power Spectrum

On the order of ten experiments have now observed CMB anisotropies. Anisotropies are observed on angular scales larger than the minimum $10'$ damping scale (see Figure 3) and are consistent with those expected from an initially scale-invariant power spectrum of potential and thus metric fluctuations. It is believed that the large scale structure in the Universe developed through the process of gravitational instability where small primordial perturbations in energy density were amplified by gravity over the course of time. The initial spectrum of density perturbations can evolve significantly in the epoch $z > 1100$ for causally connected regions (angles $\lesssim 1^\circ\ \Omega_{tot}^{1/2}$). The primary mode of evolution is through adiabatic (acoustic) oscillations, leading to a series of peaks that encode information about the perturbations and geometry of the universe, as well as information on Ω_0, Ω_B, Ω_Λ (cosmological constant), and H_0 [68]. The location of the first acoustic peak is predicted to be at $\ell \sim 220\ \Omega_{tot}^{-1/2}$ or $\theta \sim 1^\circ\ \Omega_{tot}^{1/2}$ and its amplitude increases with increasing Ω_B.

Figure 4 shows the theoretically predicted power spectrum for a sample of models, plotted as $\ell(\ell+1)C_\ell$ versus ℓ which is the power per logarithmic

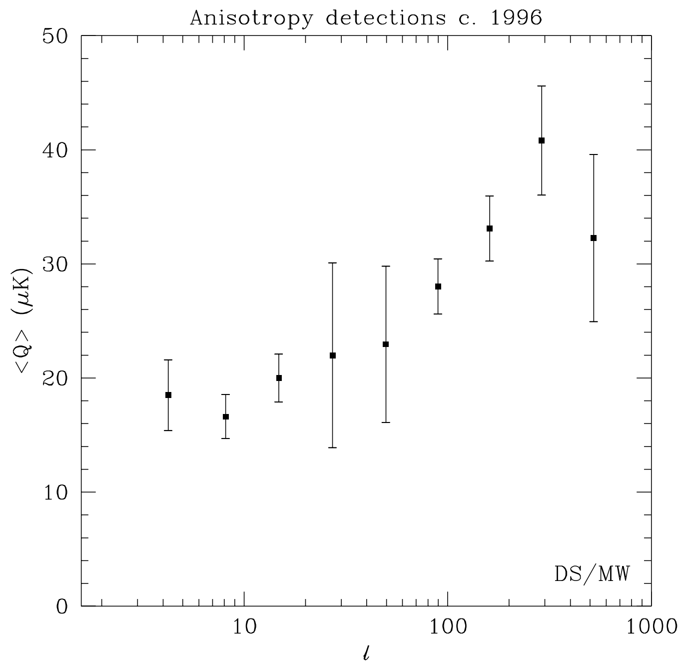

Figure 3. Current status of CMB anisotropy observations: Due to the overlapping sets of data Douglas Scott and Martin White have formed band-averages over experiments. Plotted are the quadrupole amplitudes for a scale-invariant spectrum that would give the experiment band averages. The vertical error bars represent estimates of 68% CL.

interval in ℓ or, equivalently, the two-dimensional power spectrum. If the initial power spectrum of perturbations is the result of quantum mechanical fluctuations produced and amplified during inflation, then the anisotropy spectrum and the fractional contribution from density (scalar) and gravity wave (tensor) perturbations are coupled. If the energy scale of inflation at the appropriate epoch is at the level of $\simeq 10^{16}$GeV, then detection of gravitons is possible, as well as partial reconstruction of the inflaton potential. If the energy scale is $\lesssim 10^{14}$GeV, then density fluctuations dominate and less constraint is possible. (See CMB theory lectures for more background.)

Fits to data over smaller angular scales are often quoted as the expected value of the quadrupole $\langle Q \rangle$ for some specific theory, e.g. a model with power-law initial conditions (primordial density perturbation power spectrum $P(k) \propto k^n$). The full 4-year COBE DMR data give $\langle Q \rangle = 15.3^{+3.7}_{-2.8}\,\mu$K, after projecting out the slope dependence, while the best-fit slope is $n = 1.2 \pm 0.3$, and for an $n = 1$ (scale-invariant potential perturbation) spectrum $\langle Q \rangle\,(n = 1) = 18 \pm 1.6\,\mu$K [6], [30]. The conventional notation is such that $Q^2_{\rm rms}/T^2_\gamma = 5C_2/4\pi$.

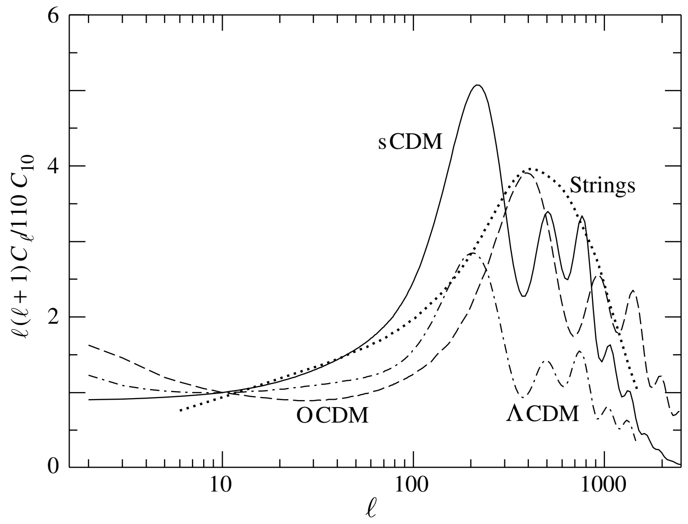

Figure 4. Examples of theoretically predicted $\ell(\ell+1)C_\ell$ or CMB anisotropy power spectra. **sCDM** is the standard cold dark matter model with $h = 0.5$ and $\Omega_B = 0.05$. **ΛCDM** is a model with $\Omega_{tot} = \Omega_\Lambda + \Omega_0 = 1$ where $\Omega_\Lambda = 0.3$ and $h = 0.8$. **OCDM** is an open model with $\Omega_0 = 0.3$ and $h = 0.75$. (See White (1996) for models). **Strings** is a model where cosmic strings are the primary source of large scale structure [1] The plot indicates that precise measurements of the CMB anisotropy power spectrum could distinguish between current models.

Only somewhat weak conclusions can be drawn based on the current smaller angular scale data (see Figure 3). However, new data are being acquired at an increasing rate. With future experiments and the prospect of next generation satellite missions: MAP and Planck, a precise measurement of the CMB anisotropy power spectrum is possible and likely, allowing us to decode the information that it contains [40],[38].

7. Current and Near-Term Experiments

Many groups have been and are working to measure the anisotropy. Though some are focussed on large angular scales at frequencies not observed with DMR, most concentrate on smaller angular scales. Table 2 contains a list for recent, current and planned experiments compiled by L. Page [58].

Rather than review all the experiments, we focus here on a representative sample.

7.1. MAX/MAXIMA/BOOMERANG

The MAX/MAXIMA/BOOMERANG payloads are representative of current and currently planned balloon-borne missions.

TABLE 2. Recently Completed, Current and Planned Anisotropy Experiments

Experiment	Resolution	Frequency	Detectors	Type	Groups
ACE(c)[86]	0.2°	25-100 GHz	HEMT	C/B	UCSB
APACHE(c)[87]	0.33°	90-400 GHz	Bol	C/G	Bologna, Bartol Rome III
ARGO(f)[88]	0.9°	140-3000 GHz	Bol	C/B	Rome I
ATCA[89]	0.03°	8.7 GHz	HEMT	I/G	CSIRO
BAM(c)[90]	0.75°	90-300 GHz	Bol	C/B	UBC, CfA
Bartol(c)[96]	2.4°	90-270 GHz	Bol	C/G	Bartol
BEAST(p)[86]	0.2°	25-100 GHz	HEMT	C/B	UCSB
BOOMERanG(p)[97]	0.2°	90-400 GHz	Bol	C/G	Rome I, Caltech, UCB, UCSB
CAT(c)[98]	0.17°	15 GHz	HEMT	I/G	Cambridge
CBI(p)[99]	0.0833°	26-36 GHz	HEMT	I/G	Caltech, Penn.
FIRS(f)[101]	3.8°	170-680 GHz	Bol	C/B	Chicago, MIT, Princeton, NASA/GSFC
HACME/SP(f)[102]	0.6°	30 GHz	HEMT	C/G	UCSB
IAB(f)[103]	0.83°	150 GHz	Bol	C/G	Bartol
MAT(p)[104]	0.2°	30-150 GHz	HEMT/SIS	C/G	Penn, Princeton
MAX(f)[105]	0.5°	90-420 GHz	Bol	C/B	UCB, UCSB
MAXIMA(p)[106]	0.2°	90-420 GHz	Bol	C/B	UCB, Rome I Caltech, UCSB
MSAM(c)[107]	0.4°	40-680 GHz	Bol	C/B	Chicago, Brown, Princeton, NASA/GSFC
OVRO 40/5(c)[108]	0.033°, 0.12°	15-35 GHz	HEMT	C/G	Caltech, Penn
PYTHON(c)[109]	0.75°	35-90 GHz	Bol/HEMT	C/G	Carnegie Mellon Chicago, UCSB
QMAP(f)[110]	0.2°	20-150 GHz	HEMT/SIS	C/B	Princeton, Penn
SASK(f)[111]	0.5°	20-45 GHz	HEMT	C/G	Princeton
SuZIE(c)[112]	0.017°	150-300 GHz	Bol	C/G	Caltech
TopHat(p)[113]	0.33°	150-700 GHz	Bol	C/B	Bartol, Brown, DSRI,Chicago, NASA/GSFC
Tenerife(c)[114]	6.0°	10-33 GHz	HEMT	C/G	NRAL, Cambridge
VCA(p)[115]	0.33°	30 GHz	HEMT	I/G	Chicago
VLA(c)[116]	0.0028°	8.4 GHz	HEMT	I/G	Haverford, NRAO
VSA(p)[117]	–	30 GHz	HEMT	I/G	Cambridge
White Dish(f)[118]	0.2°	90 GHz	Bol	C/G	Carnegie Mellon

1. For "Type" the first letter distinguishes between configuration or interferometer, the second between ground or balloon.
2. An "f" after the experiment's name means it's finished; a "c" denotes current; a "p" denotes planned, building may be in progress but there is no data yet.

7.1.1. *MAX*

The Millimeter-wave Anisotropy eXperiment (MAX) is a balloon-borne bolometric instrument which observes at multiple frequencies with high sensitivity on the 0.5° angular scale. MAX has completed five flights detecting significant CMB fluctuations [27], [2], [55], [22], [16], [74], [47].

The MAX instrument consists of an off-axis Gregorian telescope and a bolometric photometer mounted on an attitude-controlled balloon-borne platform which makes measurements at an altitude of 36 km. The Gregorian telescope consists of a 1-meter primary and a nutating elliptical secondary. The underfilled optics provides a 0.55° FWHM beam when focused and aligned. The 5.7 Hz nutation of the secondary modulates the beam on the sky sinusoidally though $\pm 0.68°$ and the attitude control sweeps the beam over a 6° or 8° path and back in about 108 seconds, producing about 15 to 20 independent temperature differences on the sky. Depending upon the time of observation and location of the region under observation sky rotation can cause the observed region to be in the shape of a bow-tie.

On flights 4 & 5 the single-pixel four-band bolometric receiver featured negligible sensitivity to radio frequency interference and an adiabatic demagnetization refrigerator to cool the photometer to 85 mK. The dichroic photometer used for MAX has $(\delta\nu/\nu)$ of 0.57, 0.45, 0.35, and 0.25 filter bands at 3.5, 6, 9, and 15 cm^{-1}. MAX covers the high frequency side of the window formed by galactic dust emission rising at higher frequencies and Galactic synchrotron and free-free emission increasing at lower frequencies. The 15 cm^{-1} channel acts as a guard against Galactic dust and atmospheric emission. The multiple frequencies have sufficient redundancy to provide confidence that the signal is CMB and not a foreground or systematic effect.

MAX is calibrated both by an on-board commandable membrane and by observations of planets, usually Jupiter. The two techniques agree at roughly the 10% level. The calibration is such that the quoted temperature difference is the real temperature difference on the sky.

MAX makes deep CMB observations (typically one hour) on regions generally selected to be low in dust contrast and total emission and free from known radio sources. MAX has made observations on five flights. The data from most of the scans are in good agreement but the scan of the μ-Pegasi region is significantly lower than the rest. A combination of all the data seems to be coming out at an intermediate value between GUM and μ-Pegasi regions and may all be consistent with coming from a single parent population [75].

The center of the scan is the same for the three observations of GUM (the star Gamma Ursae Minoris) but the relative geometry is such that the three scans made bow-tie patterns which cross at the star. White and

Bunn [79] have made use of this fact to construct a two dimensional map of the region which is roughly $10° \times 5°$. The title of their paper is "A First Map of the CMB at 0.5° Resolution". Since then a map covering 180 square degrees was generated by Tegmark et al. [78] using the Saskatoon data.

Making maps is clearly the appropriate approach for the current generation of new experiments. MAX is evolving to new systems MAXIMA and BOOMERANG, which are designed and constructed for the goal of getting the power spectrum around the first "Doppler" peak and further and making maps covering a significant portion of the sky.

7.1.2. *MAXIMA*

MAXIMA stands for MAX imaging system. The current one-dimensional scans are very useful data for the discovery phase of CMB anisotropy research. Soon progress will depend upon the availability of two-dimensional maps of low galactic foreground regions (low dust in this case) with several hundred pixels so that sampling variance is less important (see section 3). In addition one can look for properties of the sky which are not predicted by theories and could be overlooked in statistical analyses. It also makes it possible to catalog features for comparison to or motivation of other experiments.

Under the auspices of the NSF Center for Particle Astrophysics a collaboration consisting of groups from the University of California at Berkeley, Caltech, the University of Rome, and the IROE-CNR Florence have begun work and made good progress on the new systems for MAXIMA and BOOMERANG. The plan is to have a combination of northern hemisphere flights of MAXIMA and BOOMERANG and a Long Duration Balloon (LDB) flight of BOOMERANG from Antarctica.

To make an imager a new optical system was necessary. The primary mirror for MAXIMA is a 1.3-meter, off-axis, light-weight primary mirror. The primary will be modulated which allows a much larger beam chop angle on the sky with less spill over and thus more pixels in the focal plane. Cold secondary and tertiary mirrors provide a cold Lyot stop and the field-of-view required for the array of 12 arcminute pixels. The geometrical aberrations in the center of the field-of-view are less than 10 arcminutes.

A larger primary mirror requires a larger gondola which is now constructed. The chop angle can both be increased and varied allowing the instrument to sample the shape of the power spectrum over the range $40 < \ell < 1000$.

An additional feature is new detector electronics with AC coupling in order to allow linear scanning in a total power mode, making maps and power spectrum measurements directly. This approach is different than that of making a number of different window functions. The idea is to use a

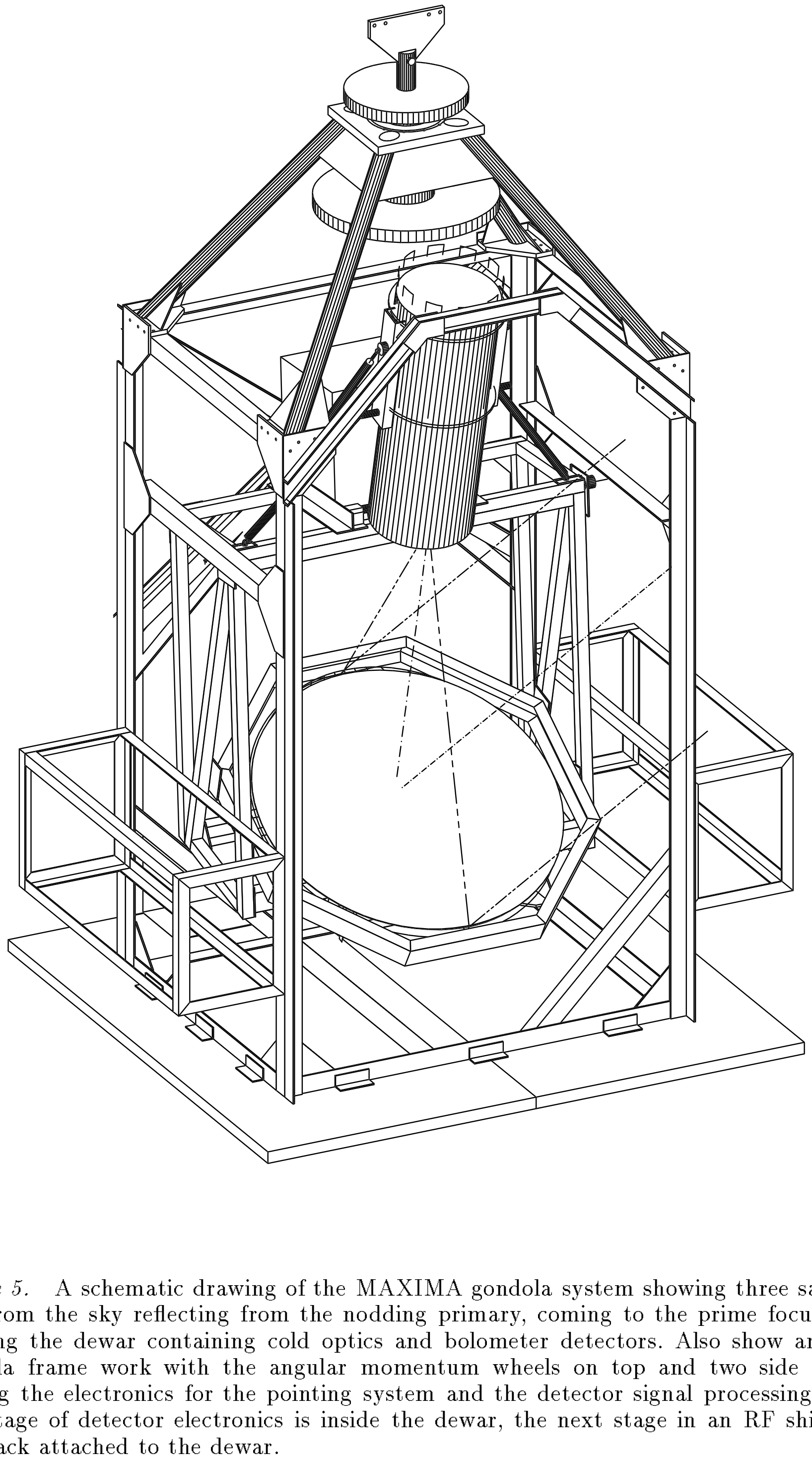

Figure 5. A schematic drawing of the MAXIMA gondola system showing three sample rays from the sky reflecting from the nodding primary, coming to the prime focus and entering the dewar containing cold optics and bolometer detectors. Also show are the gondola frame work with the angular momentum wheels on top and two side boxes holding the electronics for the pointing system and the detector signal processing. The first stage of detector electronics is inside the dewar, the next stage in an RF shielded backpack attached to the dewar.

scan or raster scan of the CMB anisotropies on the sky directly rather than obtaining a set of differences at different chop angles. One is thus mapping directly and measuring the power spectrum as the fourier transform of the data. At this stage the instrument is designed to operate in this mode by scanning the primary mirror in a sawtooth pattern rapidly (3 Hz) and more slowly moving the entire gondola in azimuth to cover a larger angle.

Another major change will be going from a single pixel four-frequency photometer to a fourteen-pixel receiver. This will allow taking data at eight times the rate and thus make two-dimensional mapping feasible. The receiver design has been completed and it and the new cold optics being mounted in the new large dewar as show in Figure 6. The bolometers have a spider-web (silicon nitride micromesh) substrate so that cosmic ray transient occurrences will be reduced by more than an order of magnitude. The first flight of the new gondola was September 1995 and we anticipate a flight with the arrary receiver in the summer/fall 1997. We can anticipate that within three years MAXIMA will have made maps and will have measured the anisotropy power spectrum around the location of the first doppler peak. Figure 7 indicates an estimate of the accuracy of the power spectrum determination.

7.1.3. *BOOMERANG*

BOOMERANG is equivalent to the long-duration balloon-borne version of MAXIMA and an intermediate step toward the bolometer space mission, the Planck HFI. Plans call for a northern hemisphere flight in June 1997 followed by a many-day flight circumnavigating Antarctica in the austral summer beginning December 1998. BOOMERANG will move more directly towards mapping a significant region of the sky. The BOOMERANG focal plane contains 8 pixels: four multiband photometers (6, 9 and 14 cm^{-1}) and four monochromatic channels (3 cm^{-1}). The diffraction limited angular resolution is $12'$ above 6 cm^{-1} and $20'$ at 3 cm^{-1}. In total power mode, the largest resolution is limited only by the length of a scan.

The high cosmic ray flux over the Antarctic requires detectors which are insensitive to cosmic rays. "Spider web" bolometers have been developed specifically to minimize the effect of cosmic rays on the detector. These bolometers are called composite because the functions of absorbing radiation and measuring the temperature increase are separated. The absorber is the "spider web" and a thermometer is a neutron transmutation doped (NTD 14) thermistor. Spider web bolometers for BOOMERANG will have a Noise Equivalent Power (NEP) of $\sim\ 1 \times 10^{-17}$ W/Hz$^{1/2}$.

The electrical circuit of BOOMERANG is split in subcircuits which reside at different temperatures. There are bolometers at 300 mK, which are AC-biased at 200 Hz and dual JFET source followers, providing a low

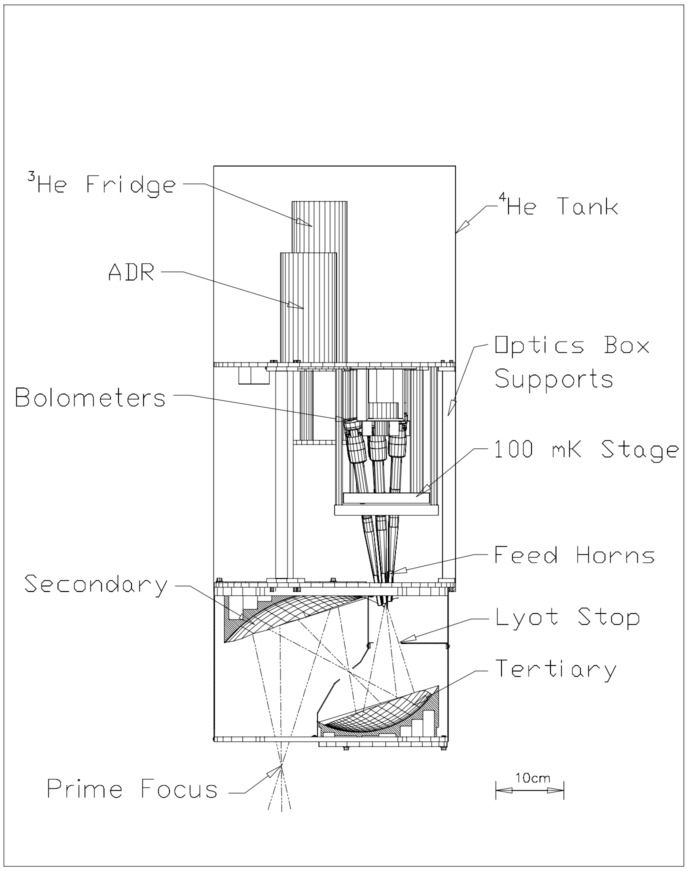

Figure 6. The cold optical system for MAXIMA. Both MAXIMA and BOOMERANG use fast off-axis LHe-cooled secondary and tertiary mirrors to reduce optics emissions. The design incorporates cold black baffles and a cold Lyot stop which controls the illumination on the primary mirror giving smaller offsets and better control of spillover than can be achieved in optical systems that are not re-imaged. The figure also shows the location of the feedhorns and the bolometers as well as the Adiabatic Demagnitization Refridgerator (ADR) and He3 fridges used to maintain the bolometers at 100 mK. The optics are shown in cross-section for clarity.

impedance line going out of the cryostat. At 300 K, the signal is preamplified, demodulated and filtered through a small bandwidth, thus enabling the detection of signals of the order of nanovolts.

The BOOMERANG North American flight will produce a map covering a region near the North Celestial Pole. It is about 10% of the full sky. This region will be mapped by sweeping in azimuth between 60 degrees and 90 degrees North latitude while holding the elevation constant; after 12 hours, the rotation of the earth will produce a map of half of a circular region centered on the NCP. The North American flight will produce the first

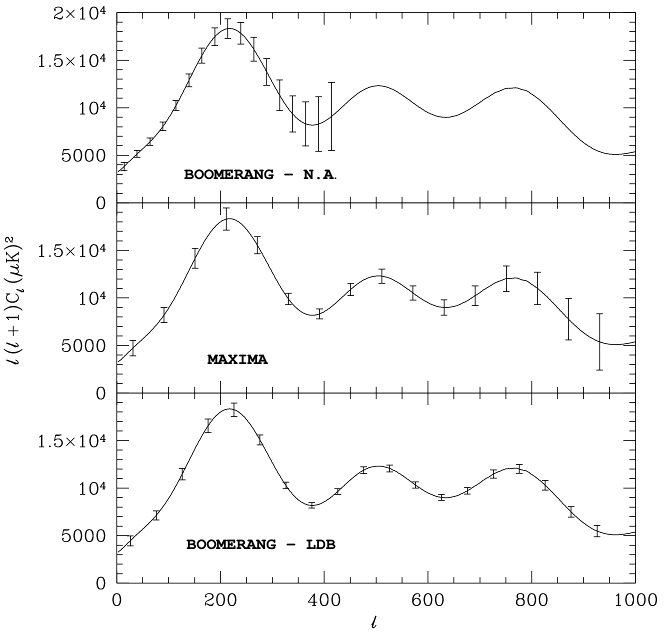

Figure 7. Estimates of the accuracy with which each of the three proposed flights for MAXIMA and BOOMERANG will determine the power spectrum of CMB anisotropy. The sold line in each frame represents the standard cold dark matter ($\Omega = 1$, $\Omega_b = 0.05$, $h = 50$, no reionization) power spectrum. The spacing of the error flags indicates the resolution provided by each experiment; the amplitude of the error flags indicate one standard deviation uncertainty and includes the effects of instrumental noise, sky coverage, and differences strategy.

total power map of a significant fraction of the northern sky.

The region to be mapped by the Antarctic flight is centered on the Southern Hole, a region of exceptionally low galactic dust emission in the southern sky. During the Antarctic summer, the anti-solar direction passes through the Southern Hole; the BOOMERANG scans will be centered on the antipode of the sun's path to minimize sidelobe response and thermal response from the sun.

The Antarctic flight will consist of three scans, each lasting five days: two fast scans of adjoining $30° \times 60°$, which cover 10% of the sky, and a deep integration of a $12° \times 12°$ subset of this region. The fast scans will result in 130 000 pixels (12 arcmin) with a sensitivity of 20 μK/pixel (thermodynamic temperature), obtained by sweeping the telescope at 1 degree/s in azimuth while varying the elevation through 40 degrees over a 24 hour period. The deep integration region will be mapped with a sensitivity of $\sim$ 10 μK/pixel. This scan will test for systematic variations in the data

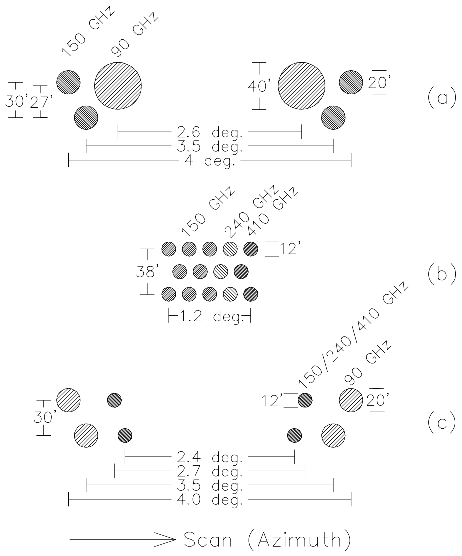

Figure 8. Layout of the three BOOMERANG and MAXIMA focal planes. The focal planes are: (a) BOOMERANG North American flight, (b) MAXIMA, and (c) BOOMERANG LDB (Antarctica). Circles indicate the relative position and FWHM of the beams projected on the sky. Each circle represents a dual-polarization, high efficiency feed, with the exception $12'$ beams shown in (c), which represent multi-frequency photometers of the type flown previously on MAX. Each experiment is scanned in azimuth, which is horizontal in the figure.

and will serve as a diagnostic for the fast scans.

BOOMERANG will complement the DMR with high sensitivity measurement of CMB power on scales between 12 arcmin and $\sim 10°$. In Figure 7, the error bars represent the $\pm 1\sigma$ limit which BOOMERANG will determine for a standard cold dark matter model. The BOOMERANG-MAXIMA program will return excellent scientific data and will be a good test of the instrumentation and techniques for Planck.

7.2. MSAM/TOPHAT

MSAM/TopHat is a collaboration working on a series of experiments to measure the medium-scale anisotropy of the cosmic microwave background radiation. The collaboration includes researchers at the Bartol Research Institute, Brown University, the University of Chicago, the Danish Space Research Institute, and NASA/Goddard Space Flight Center. MSAM/TOPHAT program is similar to MAX/MAXIMA/BOOMERANG program at present.

7.2.1. *MSAM*

MSAM is an acronym for Medium Scale Anisotropy Measurement. A notable difference between MSAM and MAX has been that MSAM used a three-position chop analyzed either as a triple beam or double beam (two chop angles on the sky) observation. MSAM angular resolution is 0.5° between 5 and 23 cm^{-1} (150 and 700 GHz or wavelengths 0.4 to 2.0 mm). MSAM has had three flights (June 1992, May 1994, June 1995) all from Palestine, Texas [15].

MSAM-I: The first phase of the Medium-Scale Anisotropy Measurement (MSAM-I) probed CMBR anisotropy at 0.5 degree angular scales between 5 and 23 cm^{-1} (150 and 700 GHz, 0.4 and 2.0 mm). The first flight of this package (June 1992 from Palestine, TX) has resulted in a detection of $0.5 \times 10^{-5} < \delta T/T < 2 \times 10^{-5}$. Fluctuations at these angular scales are believed to be the precursors of the largest structures we observe today. This level of anisotropy is at the lower end of the predicted values from standard Cold Dark Matter theories of structure formation. The interpretation of the results, however, is complicated by the presence of two point sources in the data. This hints at the possibility of a previously unsuspected population of objects which will challenge anisotropy measurements at these sensitivity levels. Such sources may be distinguished by the use of multiple spectral bands bracketing the peak of the CMBR, such as those in MSAM-I and MSAM-II. One can also interpret the two extra peaks as CMB fluctuations and then the data are in good agreement with the anisotropy predicted by SCDM.

MSAM-II is the second phase of the Medium-Scale Anisotropy Measurement. An adiabatic demagnetization refrigerator (ADR) is used to cool monolithic silicon bolometers to 100mK in a new radiometer. The new radiometer has expanded frequency coverage in 5 spectral bands between 2.3 and 5 cm^{-1} (70 to 150 GHz or wavelengths 2.0 to 4.3 mm). The instrument is expected to improve the signal-to-noise ratio by about a factor of three over the previous results.

MSAM observations are along a ring surrounding the north celestial pole with a $20'$ beam on the sky giving sensitivity to the medium angular-scale power spectrum of the radiation.

7.2.2. *TOPHAT*

TOPHAT is conceived as a long-duration balloon-borne experiment with the detectors located on the top of the balloon rather than in a gondola hanging below the balloon. The extended observation time ($\sim$2 weeks) made possible by LDB will permit a substantial fraction of the flight to be dedicated to studying and characterizing systematics in-flight while still maintaining high sensitivity to CMB anisotropy. TopHat will observe in five spectral bands between 5 and 21 cm^{-1} (150 and 630 GHz or wavelengths between 0.5 to 2.0 mm). The current plans call for the measurement of 40 points on the sky, each with an rms sensitivity of $\delta T_{rms} \approx 1$ μK or $\delta T_{rms}/T_{CMB} \approx 3 \times 10^{-7}$ including removal of the galactic foreground dust emission.

7.3. ACE/BEAST

As a follow up to their South Pole HEMT observations the Santa Barbara group has proposed ACE (Advanced Cosmic Explorer). It is a large, light-weight (200 kg), system aimed at making flights lasting 90 days or more. They plan to utilize advanced HEMTs, active refrigerators, and a 2-m diameter mirror to cover the frequency range 25 to 90 GHz. In three such flights such a system could map 75% of the sky to an angular resolution of 10 arcminutes at a level of about 20 μK. This project is still in the early phase but is indicative of what with sufficient funding one might achieve by the year 2000.

7.4. GROUND-BASED INSTRUMENTS

Ground-based instruments have made a significant contribution to CMB anisotropy observations. They have been successful as a result of the observers' clever strategies to minimize and reduce the effect of the atmosphere. These strategies have included going to high, dry sites such as the South Pole and Teide peak on Tenerife and using triple-beam chopping or other similar techniques. These techniques are more difficult to use when going to mapping and making observations over an extended portion of the power spectrum. Here again it is possible that significant progress can be made though it is likely to be eventually limited before the science is exhausted.

An exciting exception is the use of aperture synthesis interferometers. The Ryle Telescope images of the Sunyaev-Zeldovich effect in clusters and the CAT (Cambridge Anisotropy Telescope) results have convinced many that interferometers have a bright future in actually mapping anisotropy on small angular scales over selected regions of the sky.

7.4.1. *CAT: Cambridge Anisotropy Telescope; 30′ to 2°*

The CAT [64] is a three-element interferometer which can operate at frequencies between 13 and 17 GHz with a bandwidth of 500 MHz. This frequency range was chosen as a compromise between the effects of atmospheric emission, which increase with frequency, and Galactic synchrotron and bremsstrahlung emission, which decrease with frequency. The most important contaminating signal for the CAT is that from discrete extragalactic radio sources. The observation strategy is to chose fields with minimum source content and then observe the sources with the higher resolution Ryle Telescope at 15.7 GHz.

The CAT has a system temperature of approximately 50 K. Variations in the system temperature are continuously measured using a modulated 1-K noise signal injected into each antenna. The interferometer baselines can be varied from 1 to 5 m, and are scaled to give the same synthesized beam at different frequencies. The antennas have a primary beam FWHM of 2.2 degrees at 15 GHz. The CAT simultaneously records data from the two orthogonal linear polarizations. Its alt-az mount causes the plane of polarization to rotate on the sky as the telescope tracks a given field.

The CAT is situated within a 5-m high earth bank which is lined with aluminium. This shielding reduces the effect of spillover and terrestrial radio interference, but limits observations to elevations above 25 degrees. The control hut is located about 100 m away. Each element of the telescope is a corrugated-conical horn with a parabolic reflector. The horns are mounted on a single turntable which can track in azimuth. Each antenna has an individual elevation drive. Preliminary test have shown that crosstalk, correlator offsets, and antenna shadowing - particular problems associated with interferometers - do not affect the performance of the CAT at elevations greater than 40 degrees [65], [56]. Results [35] are shown in the summary figure of anisotropies.

7.4.2. *Interferometers: VSA, CBI, & VCA*

Three major interferometer projects are funded and underway. They are the VSA (Very Small Array, $15'$ to $4°$) in England, the Caltech interferometer CBI (Cosmic Background Interferometer, $4'$ to $20'$) and the University of Chicago VCA (Very Compact Array, $15'$ to $1.4°$). These interferometers are likely to provide a very good first look at the CMB anisotropy power spectrum on angular scales less than about $0.5°$ ($\ell > 200$).

VSA is a joint project between the Mullard Radio Astronomy Observatory (Cambridge), the Nuffield Radio Astronomy Laboratories (Jodrell Bank, Manchester), and the Instituto de Astrofisical de Canarias (Tenerife). The VSA is similar in design to CAT which was a prototype for VSA. The VSA will have 15 antennas and a 2-GHz bandwidth, analog correlators, and other technology operated on CAT. The operating frequency is 26-36 GHz which is set by the atmospheric window and the natural waveguide bands for which high sensitivity HEMT amplifiers have been developed. The increase in frequency from CAT to VSA will also decrease the effect of discrete radio sources and Galactic emission. The atmospheric emission fluctuations will increase so that VSA will be operated on Mt. Teide on the island of Tenerife. The VSA will operate with two sets of horns: one

TABLE 3. Characteristics of Next Generation Interferometers

Initials:	VSA	VCA	CBI
Name:	Very Small Array	Very Compact Array	Cosmic Background Imager
Frequency (GHz)	28 - 37	26 - 36	26 - 36
N_a	14, 15	13	13
No. of Channels	1 tunable	10	10
T_{sys} (K)	$\sim$25	$\sim$25	$\sim$25
$\Delta\nu$	1.75	1	1
ℓ range	150-1600	150-750	400-3500
Resolution	$15'$	$15'$	$4.5'$
Site	Tenerife	Anarctica	California, Chile
Point Sources	Ryle & Bonn	A. T.	VLA & 40-m
Correlations	analog	analog	analog
Operational	1999	1999	1999

set with a 15-cm aperture giving a 4° field of view and the second with a 30-cm aperture giving a 2° field of view. The baselines and thus resolution will scale proportionally to maintain about a 1 μK sensitivity per resolution element. The VSA will get about 10 independent points of the anisotropy power spectrum with resolution of $\Delta\ell = 100$ at low ℓ and $\Delta\ell = 200$ at high ℓ covering the range $130 < \ell < 1800$.

The CBI and VCA are planning to observe the same portion of sky in the southern hemisphere. The proposed VCA is expected to image about 2500 square degrees around the South Pole region and if that goes well continued operation to cover eventually about 25% of the sky. The VCA interferometer consists of 13 scalar feed horns arranged in a closed packed configuration which fill about 50% of the aperture to provide maximum brightness sensitivity. The horns feed low-noise HEMT amplifiers operating at 26 to 36 GHz with noise temperatures of about 10 K. The estimated sensitivity is 4 to 10 μK in pixels ranging from 0.25° to 1.4° in the 3° field of view. The VCA will be operated from the South Pole Station and is scheduled for installation in the fall of 1998 with first results expected the following spring.

The sensitivity of an interferometer system can be estimated using the following formulae for flux density and temperature:

Flux density

$$\Delta S_{rms} = \frac{2kT_{sys}}{\eta_a A_a \eta_c [n_a(n_a-1)\Delta\nu\tau]^{1/2}}$$

Temperature

$$\Delta T_{rms} = \frac{\lambda^2 T_{sys}}{\theta_s^2 \eta_a A_a \eta_c [n_a(n_a-1)\Delta\nu\tau]^{1/2}}$$

Same expressions evaluated with typical numbers:
Flux density

$$\Delta S_{rms} = \frac{6(\frac{T_{sys}}{30\ K})}{(\frac{\eta_a}{0.6})(\frac{d}{20\ cm})^2(\frac{\eta_c}{0.9})[\frac{n_a}{14}\frac{n_a-1}{13}\frac{\Delta\nu}{10^9}\frac{\tau}{1\ month}]^{1/2}}\mathrm{mJy}$$

Temperature

$$\Delta T_{rms} = \frac{6(\frac{\lambda}{1\ cm})^2(\frac{T_{sys}}{30\ K})}{(\frac{\theta_s}{20'})^2(\frac{\eta_a}{0.6})(\frac{d}{20\ cm})^2(\frac{\eta_c}{0.9})[\frac{n_a}{14}\frac{n_a-1}{13}\frac{\Delta\nu}{10^9}\frac{\tau}{1\ month}]^{1/2}}\mu K$$

One can then evaluate these formula and compare with the table to estimate the sensitivity and sky area that can be surveyed in a given observing time and see that on small angular scales interferometers are competive with many other experiments.

8. Future Satellite Missions

An accurate, extensive imaging of CBR anisotropies with sub–degree angular resolution would provide decisive answers to several major open questions on structure formation and cosmological scenarios. The observational requirements of such an ambitious objective can be met by a space mission with a far–Earth orbit and instruments based on state–of–the–art technologies.

While balloon-borne and ground-based observations can do a credible job in measuring the CMB anisotropy power spectrum, atmospheric disturbance, emission from the Earth and limited integration time are the main limiting factors which prevent ground–based and balloon–borne experiments from obtaining sufficient sensitivity over very large sky regions, with additional difficulties in reaching accurate foreground removal (see Danese et al. 1995 for a recent discussion). Only a suitably designed space mission can meet the scientific goals sought by cosmologists. On the other hand it should be stressed that experiments from the ground or from balloons are not alternative to a space mission like Planck, but rather complementary.

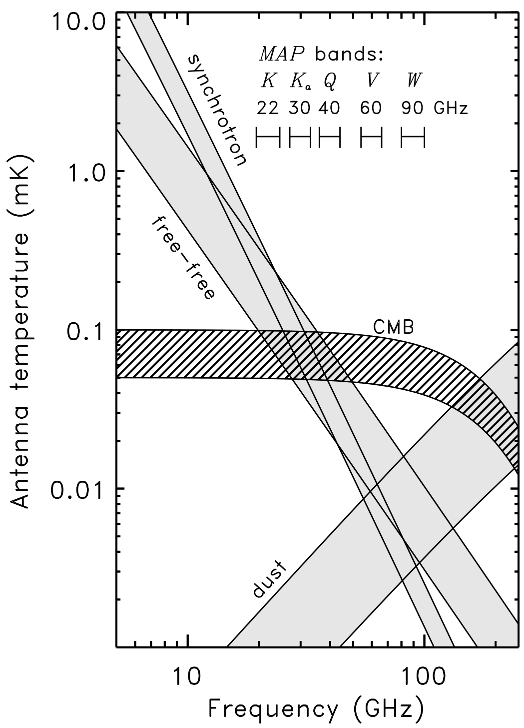

Figure 9. Galactic Foreground Emission estimates plotted as a function of frequency. The width of the band indicates the estimated range for Galactic latitudes varying between $20° < b < 70°$. The proposed MAP frequency bands are indicated.

8.1. **MAP**

MAP (Microwave Anisotropy Probe) has been selected by NASA in 1996 as a MidEX class mission. Its launch is expected to be roughly 2001. The goal of MAP is to measure the relative CMB temperature over the full sky with an angular resolution of 0.3°, a sensitivity of 20 μK per 0.3° square pixel, and with systematic effects limited to 5 μK per pixel. Details about the major aspects of the mission design are given below.

8.1.1. *Galactic Emission Foreground*

Galactic foreground signals are distinguishable from CMB anisotropy by their differing spectra and spatial distributions.

Figure 9 shows the estimated spectra of the Galactic foreground signals and a range of expected cosmological signal intensities. The three physical mechanisms that contribute to the Galactic emission are synchrotron radiation, free-free radiation, and thermal radiation from interstellar dust. Results from CMB and other measurements show that at high Galactic latitudes CMB anisotropy dominates the Galactic signals in the range 30-150 GHz. However, the Galactic foreground will need to be measured and removed from some of the MAP data.

There are two techniques that MAP will use to evaluate and remove the Galactic foreground. The first uses existing Galactic maps at lower (radio) and higher (far-infrared) frequencies as foreground emission templates. Uncertainties in the original data and position-dependent spectral index variations introduce errors with this technique. There is no good free-free emission template because there is no frequency where it dominates the microwave emission. High resolution, large scale maps of H-alpha emission will be a template for the free-free emission when they become available. One surprise has been the apparent correlation between free-free emission and dust infrared emission, sometimes more so than to H-alpha emission. This indicates that we may not yet have a template for free-free emission.

The second technique is to form linear combinations of multi-frequency MAP observations such that signals with specified spectra are cancelled. The linear combination of multi-frequency data makes no assumptions about the foreground signal strength or spatial distribution, but requires knowledge of the spectra of the foregrounds. Both techniques were successfully employed by COBE.

The contamination from extragalactic radio sources is not yet a solved issue. Flat spectrum radio sources observed with a diffraction limited system produce a signal with very nearly the same frequency dependence as the CMB anisotropy making the spectral shape technique ineffective. It will be necessary to compile a list of significant radio sources and excise them from the data or find another approach.

Five frequency bands with comparable sensitivity are desirable to solve for the four signals (synchrotron, free-free, dust, and CMB anisotropy) and the fifth degree of freedom is used to maximize signal-to-noise. The range of frequency coverage is more important than the specific choice of frequencies within the range. The lowest frequency to survey from space should be at the 22 GHz atmospheric water line since frequencies below this can (with difficulty) be accurately measured from the ground. The highest frequency to survey should be about 100 GHz to reduce the dust contribution and minimize the number of competing foreground signals. The choice of frequencies between 22 and 100 GHz can be dictated by the practical consideration of standard waveguide bands. Based on these considerations, MAP has selected the five frequency bands, which are indicated Figure 9 and in Table 2.

8.1.2. *MAP Mission Goals*

CMB anisotropy information from current and proposed high resolution ($< 0.3°$) measurements over limited sky regions will likely succeed from ground and balloon-based platforms. The priority for the MAP mission is to map the entire sky with $> 0.3°$ angular resolution where the cosmological return is high, and the data cannot be readily obtained in any other way. The MAP optics feature back to back 1.5-meter primary reflectors which lead to an angular resolution of 0.29° in the highest frequency (90 GHz) channel.

The following table gives the angular resolution to be obtained from each of the five MAP frequency bands. The value quoted is the full width at half maximum (FWHM) of the approximately Gaussian central beam lobe, in degrees.

TABLE 4. MAP Angular Resolution

Frequency (GHz)	Band Name	Wavelength (mm)	Beam Spec	FWHM Design	No. of Channels	Sensitivity 0.3° by 0.3° pixel
22 GHz	K band	13.6	0.90°	0.93°	4	35μK 26μK
30 GHz	Ka band	10.0	0.65°	0.68°	4	35μK 32μK
40 GHz	Q band	7.5	0.53°	0.47°	8	35μK 27μK
60 GHz	V band	5.0	0.39°	0.35°	8	35μK 35μK
90 GHz	W band	3.3	0.29°	0.21°	16	35μK 35μK

The MAP specification calls for an equal noise sensitivity per frequency band of 35 μK per $0.3° \times 0.3°$ square pixel. The mission duration required to meet this specification is one year of continuous observation. If Galactic emission is negligible at high latitudes above 40 GHz, as was the case for COBE, the sensitivity achievable by combining the three highest frequency channels is 20 μK per $0.3° \times 0.3°$ pixel.

The corresponding sensitivity to the angular power spectrum, obtained with simple analytic formulae, is illustrated in Figure 10 which shows the predicted power spectra for a number of competing structure formation models. The gray band straddling the solid (CDM) curve indicates the MAP sensitivity after combining the three highest frequency channels and averaging the spectrum over a 10% band in spherical harmonic order.

8.1.3. *MAP Trajectory and Orbit*

To minimize environmental disturbances and maximize observing efficiency, MAP will observe from a Lissajous orbit about the L2 Sun-Earth Lagrange

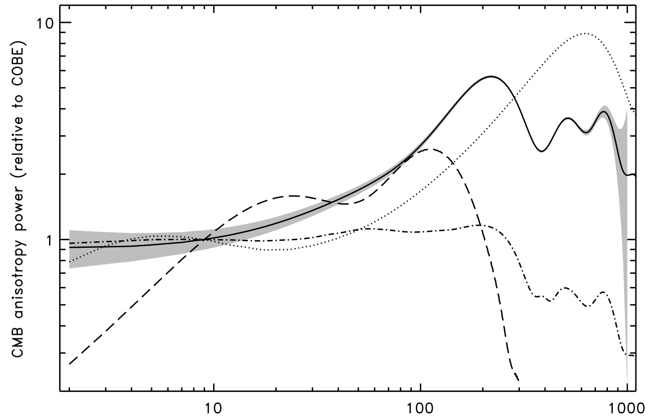

Figure 10. Projected MAP Power Spectrum Sensitivity. This plot shows a simple-minded estimate of the MAP sensitivity in measuring the CMB power spectrum. The gray band straddling the solid (CDM) curve indicates the MAP sensitivity after combining the three highest frequency channels and averaging the spectrum over a 10% band in spherical harmonic order. The curves plotted correspond to a standard CDM model (solid), a highly reionized CDM model (dot-dash), an open CDM model (dotted), and a primordial baryon isocurvature (PBI) model (dashed).

point 1.5 million km from Earth. The trajectory selected to attain such an orbit consists of 2.5-3.5 lunar phasings loops followed by about a 100 day cruise to L2. No thruster firings are required to enter the L2 orbit.

The L2 Lagrange point offers a virtually ideal location from which to carry out CMB observations. Because of its distance, 1.5 million km from Earth, it affords great protection from the Earth's microwave emission, magnetic fields, and other disturbances. It also provides for a very stable thermal environment and near 100% observing efficiency since the Sun, Earth, and Moon are always behind the instrument's field of view.

The following description indicates the path MAP will follow to L2. The trajectory features 2.5 or 3.5 lunar phasing loops which assist the spacecraft in reaching L2. The cruise time to L2 is approximately 100 days after the lunar phasing loops are completed. The launch window for this trajectory is about 20 minutes/day for 7 consecutive days each month. Once in orbit about L2, the satellite maintains a Lissajous orbit such that the MAP-Earth vector remains between 1° and 10° off the Sun-Earth vector to satisfy communications requirements while avoiding eclipses. Station-keeping maneuvers will be required about 4 times per year to maintain this orbit.

8.1.4. *MAP Instrumentation*

The MAP instrument consists of two back to back, off axis Gregorian telescopes that produce two focal planes, A and B, on opposite sides of the spacecraft symmetry axis. A set of 10 corrugated feeds lie in each focal plane and collect the signal power that goes to the amplification electronics. The microwave system consists of 10 4-channel differencing assemblies that are designed to eliminate low frequency gain instabilities and amplifier noise in the differential signal.

The reflector design incorporates two back-to-back off-axis Gregorian telescopes with 1.5-m primary reflectors and 0.52 m secondary reflectors. Each primary is an elliptical section of a paraboloid, while the secondaries are nearly elliptical. This arrangement produces two slightly convex focal surfaces on opposite sides of the spacecraft spin (symmetry) axis with plate scales of about $15'$/cm. The 99.5% encircled energy spot size diameter is less than 1 cm over a 15 x 15 cm region of the focal plane, and less than 0.33 cm over the central 8 x 8 cm region.

In order to limit diffracted signals to less than 0.5 μK, diffraction shields are employed above, below, and to the sides of each secondary. In addition, the deployable solar panels and multi-layer insulation guarantee that the secondaries remain at least $6°$ into the shadow from the Sun during observing.

The feed design calls for as small an aperture as possible consistent with a primary edge taper requirement of -25 dB, and a length that places the throat of each differential feed pair in close proximity to the other. The feed aperture diameters scale inversely with frequency, while the primary is equally illuminated at each frequency, leading to a frequency dependent beam size. The feeds are corrugated to produce beams with high symmetry, low-loss, and minimal sidelobes: the extremely low loss HE_{11} hybrid mode dominates. The phase center of each feed is kept as close as possible to its aperture, resulting in a frequency-independent beam for each feed. Since the distance from the focal plane to the spacecraft symmetry axis is nearly the same for all the feeds, the high frequency feeds are extended with low loss corrugated waveguide, while the low frequency feeds are "profiled" to reduce their length, while limiting excitation of the TE_{11} mode to less than -30 dB.

The microwave system consists of 10 4-channel differencing assemblies, one for each pair of feeds. One assembly operates at 22 GHz, one at 30 GHz, two at 40 GHz, two at 60 GHz, and four at 90 GHz. The base of an A-side feed in the Focal Plane Assembly (FPA) is attached to a low-loss orthomode transducer (OMT) which separates the signal into two orthogonal polarizations, A and A'. The A side signal is differenced against the orthogonal polarization, B', from the corresponding B-side feed, and vice-versa.

The differencing is accomplished by first combining the two signals A and B' in a hybrid tee to form $(A+B')/\sqrt{2}$ and $(A-B')/\sqrt{2}$, then amplifying each in two cold HEMT amplifiers and sending the phase-matched outputs to the warm receiver box via waveguide. The two signals are amplified in

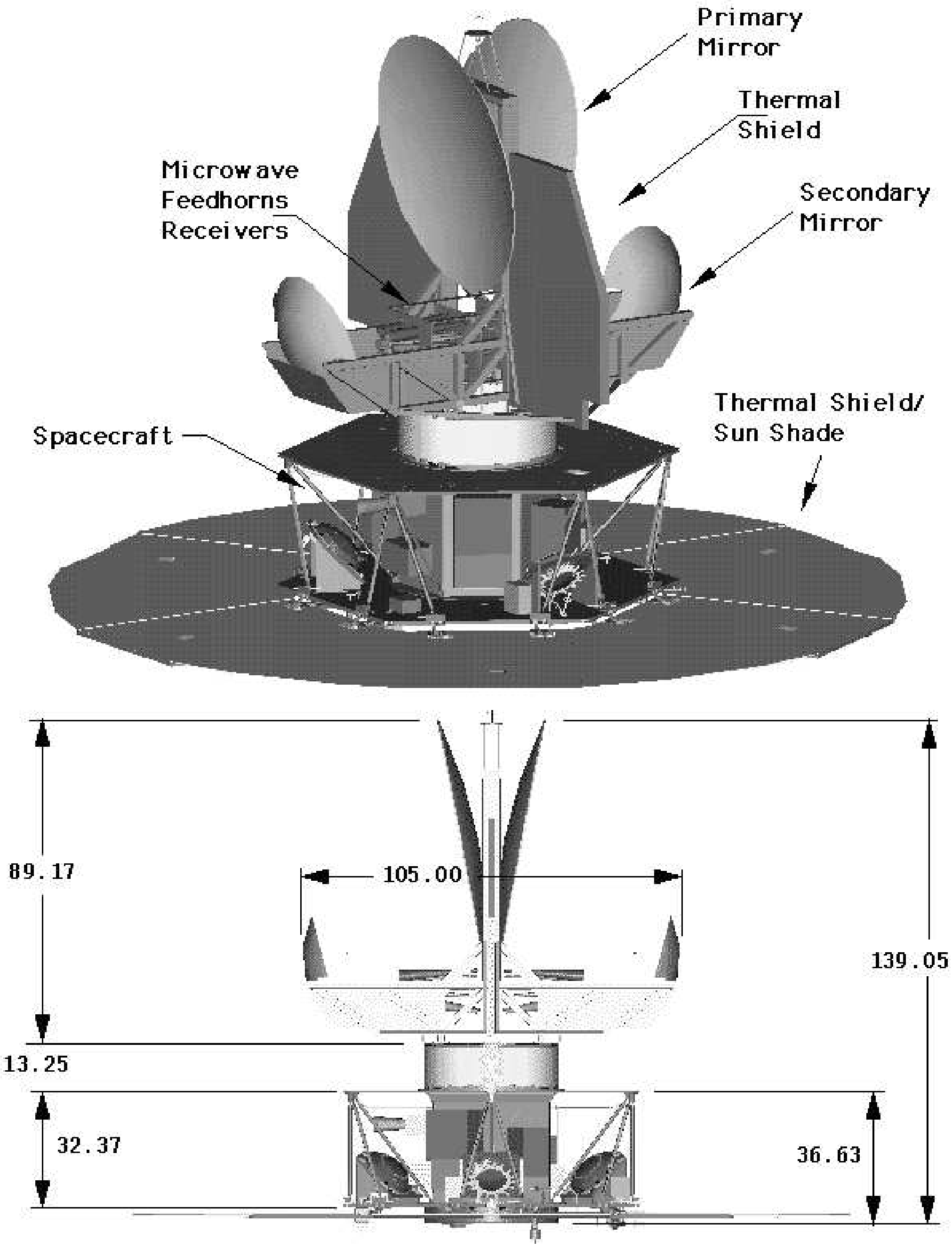

Figure 11. MAP (Microwave Anisotropy Probe) artists conception shown in two views.

two warm HEMT amplifiers, phase switched between 0° and +90° or -90°, respectively, at 2.5 kHz, then split back into A and B′ in a second hybrid tee. At this point, the two signals are square-law detected, amplified by two line drivers, and sent to the Analog Electronics Unit for synchronous demodulation and digitization. The other pair of signals, A′ and B, are differenced in the same manner giving a total of four amplification channels per differencing assembly.

The splitting, phase switching, and subsequent combining of the signals enhances the instrument's performance in two ways:

(1) Since both signals to be differenced are amplified by both amplifier chains, gain fluctuations in either amplifier chain act identically on both signals and thus cancel upon differencing. (2) The phase switches introduce a 180 degree relative phase change between the two signal paths, thereby interchanging which signal is fed to which square law detector. Thus, low frequency noise from the detector diodes is common mode and also cancels, further reducing susceptibility to systematic effects.

8.1.5. *Map Making with Differential Data*

MAP will observe temperature differences between points separated by 135° on the sky. Maps of the relative sky temperature will be produced from the difference data by a modification of the algorithm used by COBE-DMR.

The algorithm MAP will use to reconstruct sky maps from differential data is iterative. It is mathematically equivalent to a least squares fitting of the temperature differences to the map pixel temperatures. However, the scheme has a very intuitive interpretation: for a given pair of differential feeds, A and B, the A feed can be thought of as viewing the sky while the B feed can be thought of as viewing a comparative reference signal, or vice versa. In MAP's case, the comparative signal is a different point in the sky. The actual signal MAP measures is the temperature difference between two points on the sky, $\Delta T = T(A)-T(B)$, where T(A) is the temperature seen by feed A, and likewise for B. If the temperature T(B) is known, one could recover T(A) using $T(A) = \Delta T+T(B)$, but since T(B) is not known, the algorithm makes use of an iterative scheme in which T(B) is estimated from the previous sky map iteration. Thus the temperature in a pixel of a map is given by the average of all observations of that pixel after correcting each observation for the estimated signal seen by the opposite feed.

For this scheme to be successful it is imperative for a given pixel to be observed with many different pixels on its ring of 135° partners away. Thus the method requires a carefully designed scan strategy. The MAP strategy achieves this while simultaneously avoiding close encounters with the Sun, Earth, and Moon. The algorithm has been tested with the MAP scan strategy using an end-to-end mission simulation that incorporates a realistic sky signal, instrument noise, and calibration methods. The results of these simulations are described in detail in an Astrophysical Journal article [84]. After 40 iterations of the algorithm, the artifacts that remain in the map due to the map-making itself have a peak-peak amplitude of less than 0.2 μK, even in the presence of Galactic features with a peak brightness in excess of 60 mK.

8.1.6. *MAP Sky Coverage and Scan Strategy*

MAP will observe the full sky every six months. The MAP scan strategy combines spacecraft spin and precession to achieve the following: 1) The MAP instrument observes more than 30% of the sky each day; 2) The spacecraft spin (and symmetry) axis maintains a fixed angle of 22.5° from the Sun-Earth line to mitigate systematic effects; and 3) Each sky pixel is connected to thousands of other sky pixels to ensure high quality map solutions with negligible noise correlations.

Since a major goal of cosmology is to determine the statistical properties of the universe, it is clear that the largest possible number of sky samples improves constraints on cosmological models. The measurement of each individual position on the sky is an independent sample of the cosmology of the universe. Moreover, full sky coverage is absolutely required to accurately determine the low-order spherical harmonic moments. While the largest angular scales were observed by COBE, MAP will remeasure the full sky with higher resolution to:

- Avoid relative calibration errors when two or more experimental results are combined (eg., COBE and MAP).
- Provide greater sensitivity to the angular power spectrum.
- Independently verify the COBE results.

The goals of the MAP scan strategy include the following:

The angular separation between the two observing beams should be "large" in order to maintain sensitivity to signal at large angular scales. This is important for comparing the MAP results to COBE, for properly normalizing the angular power spectrum, and for retaining sensitivity to the dipole which will serve as MAP's primary calibration source.

- Observe a large fraction of the sky every day. This guarantees that sky pixels will be observed at many different times in the mission which provides the capability to monitor instrument stability on many different time scales.
- Maintain a fixed angle between the spacecraft spin axis and the local solar vector. This provides for stable illumination of the spacecraft solar panels which lie normal to the spin axis, and provides a thermally stable environment to mitigate systematic effects.

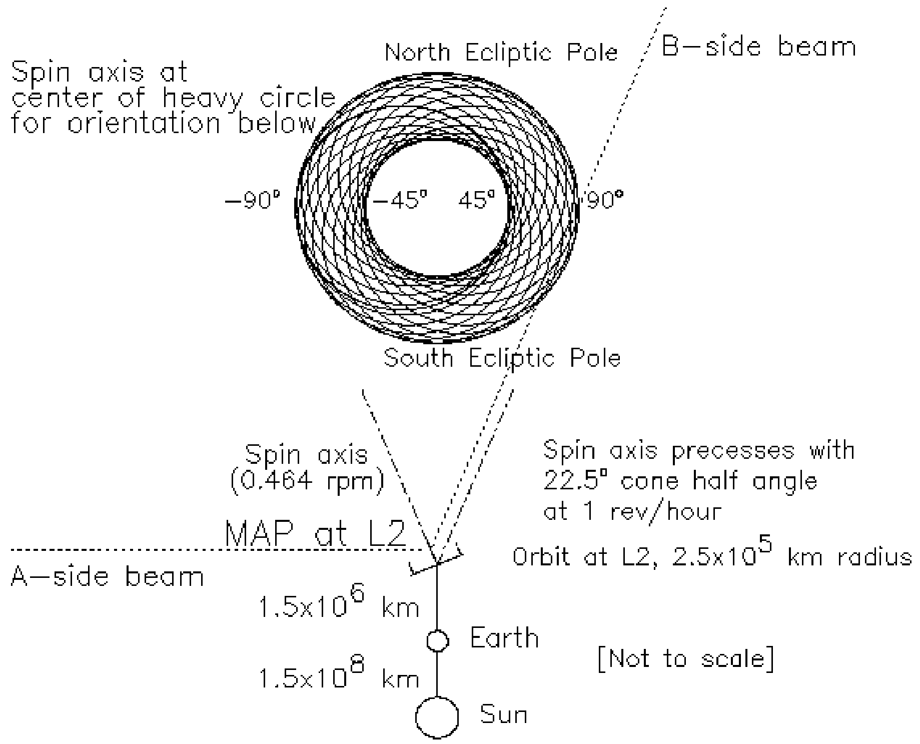

Figure 12. The MAP scan pattern for one hour of observation. The lines show the path for one side of a differential antenna pair. The other pair member follows a similar path, only delayed by 1.1 min. There are four principal time scales for the observations. The phase of the difference signal is switched by 180° at 2.5 KHz. The spacecraft spins around its symmetry axis with a 2.2 min period (bold circle) with cone opening angle of roughly 135°. This pattern precesses about the Earth-Sun line with a period of 60 minutes. Thus, in about 1 hour, over 30% of the sky is covered. Every six months, the whole sky is observed. Note that any pixel is differenced to another pixel in many directions.

• Connect each sky pixel to as many other sky pixels as possible to provide high quality map solutions from the differential data, and to render negligible pixel-pixel noise correlations. Since the MAP beam separation is fixed, this implies observing as many pixels on the differential ring of pixels as possible.

The MAP beam separation is 135°. Each beam axis points 67.5° away from the spin and symmetry axis of the spacecraft. The spin axis will precess in a 22.5° angle about the local solar vector. The combined spacecraft spin and precession will cause the observing beams to fill an annulus centered on the local solar vector with inner and outer radii of 45° and 90° respectively. Thus MAP will observe more than 30% of the sky each day and will observe the ecliptic poles every day. The spin period will be 2.2 minutes while the precession period will be 1 hour. As the Earth orbits the Sun, the whole observing annulus revolves with it producing full sky coverage.

The MAP mission is moving ahead quickly. Its spacecraft preliminary design review occurred in January 1997 and instrument held in March 1997. At that point many of the major design features were fixed and only smaller modifications will occur. However, MAP has a WWW page http://map.gsfc.nasa.gov which can be consulted for the latest information.

8.2. PLANCK – THE THIRD GENERATION SPACE MISSION

The Planck mission is the result of the merging of two proposals presented in 1993 to the European Space Agency *M3 Call for Mission Ideas*: COBRAS (Cosmic Background Radiation Anisotropy Satellite [52] and SAMBA (Satellite for Measurements of Background Anisotropies [63]). The COBRAS/SAMBA team completed the ESA assessment study in May 1994, and the project continued and completed the Phase A study in May 1996. COBRAS/SAMBA, renamed Planck Surveyor, has been selected to continue within the European Space Agency M3 programme.

The Planck mission is designed for extensive, accurate mapping of the anisotropy of the CMB, with angular sensitivity from sub–degree ($\sim 8'$–$30'$) scales up to the full sky thus overlapping with the COBE–DMR maps and with signal sensitivity approaching $\Delta T/T \sim 10^{-6}$. Planck will survey the entire sky at frequencies from 30 to 850 GHz ($1\,\mathrm{cm} \leq \lambda \leq 350$ microns). Its 1.3-m passively cooled telescope will be diffraction limited at frequencies below 375 GHz. The primary science goal is a definitive measurement of the structure in the CMB on all angular scales of $10'$ or larger. The case for orbital measurements of CMB anisotropy has been well made. An accurate measurement of CMB anisotropy with angular resolution of $10'$ will revolutionize cosmology. A full description of the baseline Planck mission is available from ESTEC at http://astro.estec.esa.nl/SA-general/Projects/ COBRAS/cobras.html. Additional information is available at http://aether.lbl.gov/www/cosa/ This information will be updated regularly and new links added.

Planck has been selected as ESA's next medium-scale mission (M3), this was confirmed in the November 1996 review of the Ariane V demise of the Cluster Mission. Planck is scheduled to fly in 2004, approximately four years after the MAP NASA Midex mission. Planck is well-designed to follow MAP. Using more sophisticated detector technology, Planck will have 10 times the sensitivity, 2 or 3 (depending on frequency) times the angular resolution, and 6 times the frequency coverage of MAP. This performance will allow Planck to:

1. Measure the power spectrum of the CMB with accuracy limited by cosmic variance over almost the entire range of angular frequency space in which useful cosmological information is expected.

2. Separate Galactic and extragalactic foregrounds from the CMB with high accuracy and confidence. The broad frequency coverage will allow determination of all important foreground components without any prior assumptions about their spectra.

3. Separate secondary anisotropies due to the Sunyaev-Zel'dovich effect from primary anisotropies, and measure the SZ effect with precision in thousands of clusters of galaxies. This information, combined with X-ray data, will yield an independent measurement of the Hubble constant on large scales and probe the peculiar velocity field of clusters to high redshift.

4. Separate polarization of the CMB from that in local foregrounds and measure it with precision on angular scales as small as $7'$.

5. Survey the sky at sub-mm (350, 550 and 850 microns) wavelengths that complement the wavelength coverage of SIRTF. The chance for serendiptous discovery in this survey is great.

Planck has two instruments: the Low Frequency Instrument (LFI), based on transistor (HEMT) amplifiers, which covers the frequency range from 30–100 GHz; and the High Frequency Instrument (HFI), based on bolometers, which covers the frequency range 90–850 GHz. The implementation of these technologies fits comfortably within the mass, power, volume and schedule constraints of the ESA M3 opportunity.

8.2.1. *Planck Active Cooling Option*

One area being pursued at the present is the use of actively cooled HEMTs, which requires the HEMT amplifier chain to be broken into a low-temperature portion and a higher-temperature portion. This split reduces the thermal load on the focal plane allowing passive cooling to a significantly lower temperature (i.e., 65 K) and allowing for the use of active cooling technologies such as a hydrogen sorption cooler.

In addition, there are technical advantages of a combined LFI/HFI focal assembly that uses a hydrogen sorption cooler to cool both the HEMTs and the 20 K shield of the bolometer dewar. The sorption cooler would replace the 20 K Stirling cooler in the baseline design, with its attendant problems in vibration and instrument integration, and reduce the overall mass and power of the instruments. This is an extremely attractive option that will be studied in detail by both the HFI and LFI teams.

The split HEMT design and sorption cooler enable a LFI design with the following features:

• An increase in the sensitivity of the LFI by a factor of roughly five at the highest frequency over that of the Phase A baseline design.

• Division of the HEMT radiometers into a cold focal assembly and a room-temperature assembly. The power dissipated in the focal assembly is more than an order of magnitude lower than assumed in the Phase A study design, allowing radiative cooling of the focal assembly to a temperature of $\leq 65\,$K instead of $\sim 100\,$K.

• Active cooling of the HEMTs in the focal assembly to $\leq 20\,$K. This reduces potential thermal interactions between the LFI and HFI.

• Elimination of the $\sim 80\,$K Stirling cooler in the baseline design.

• The option (introduced above) of using the sorption cooler to cool the 20 K shield around the HFI as well as the HEMTs, eliminating the need for the 20 K Stirling cooler in the baseline design. An important benefit of this option is that the vibration associated with Stirling coolers would be eliminated from the focal assembly. The overall mass and power requirements of the instruments on the spacecraft would decrease by roughly 25 kg and 100 W as well.

This design will allow a full identification of the primordial density perturbations which grew to form the large–scale structures observed in the present universe. The Planck maps will provide decisive answers to several major open questions relevant to the structure formation epoch and will provide powerful tests for the inflationary model as well as several astrophysical issues. Planck will utilize a combination of bolometric and radiometric detection techniques to ensure the sensitivity and wide spectral coverage required for accurate foreground discrimination. An orbit far from Earth has been selected to minimize the unwanted emission from the Earth as a source of contamination.

8.2.2. *Planck Scientific Objectives*

The Planck mission will produce near all-sky maps of the background anisotropies in 8 frequency bands in the range 30–800 GHz, with peak sensitivity $\Delta T/T \sim 10^{-6}$. The maps will provide a detailed description of the background radiation fluctuations. Individual hot and cold regions should be identified above the statistical noise level, at all angular scales from $\lesssim 10'$ up to very large scales, thus providing a high resolution imaging of the last scattering surface.

The Planck maps will provide all multipoles of the temperature anisotropies from $\ell = 1$ (dipole term) up to $\ell \simeq 1500$ (corresponding to $\sim 7'$). It is the information contained in this large number of multipoles that can probe the various proposed scenarios of structure formation and the shape of the primordial fluctuation spectrum (for comparison, the COBE–DMR maps are limited to $\ell \lesssim 20$).

Table 3 compares the ability of various CMB missions to determine cosmological parameters in a model-dependent but self-consistent way. The details of the calculation are not important, with two exceptions. First, $\Omega = 1$ was assumed. If Ω is smaller differences in angular resolution become even more important. Second, it was assumed that confusing foregrounds were completely removed. In practice this will not be the case. The advantage that Planck's wide frequency coverage gives is therefore not reflected in the table. Nevertheless, the power of Planck in general, and the advantages of cooling the HEMTs, are immediately apparent.

TABLE 5. UNCERTAINTIES IN COSMOLOGICAL PARAMETERS

PARAMETER	INSTRUMENT MAP	C/S HFI[a]	C/S LFI[b]	C/S LFI[c]
$Q_{\mathrm{rms-ps}}/20\mu K$	0.23	0.12	0.18	0.14
h	0.13	0.032	0.12	0.065
$h^2\Omega_b$	0.0072	0.0019	0.0062	0.0036
Ω_Λ	0.67	0.19	0.59	0.33
Ω_ν	0.38	0.12	0.36	0.28
Ω	0.11	0.012	0.068	0.029
n_s	0.12	0.017	0.074	0.029
τ	0.35	0.15	0.26	0.20
N_ν	0.43	0.16	0.40	0.26
T_0 μK	0.01	0.01	0.01	0.01
Y	0.01	0.098	0.01	0.01
T/S	0.47	0.17	0.28	0.19
$Q_{\mathrm{ps}}/0.2\mu K$	0.02	0.000021	0.06	0.0006
$Q_{\mathrm{diffuse}}/20\mu K$	0.19	0.17	0.18	0.18

[a] HFI based on "spider web" bolometers, as given in Phase A study

[b] LFI based on InP HEMTs at 100 K, as given in Phase A study

[c] LFI based on InP HEMTs at 20 K

The high resolution Planck maps will provide a key test for structure formation mechanisms, based on the statistics of the observed $\Delta T/T$ distribution. The inflationary model predicts Gaussian fluctuations for the statistics of the CBR anisotropies, while alternative models based on the presence of topological defects, such as strings, monopoles, and textures, predict non–Gaussian statistics (e.g. [19]). Due to the different nature of their early history causality constrains primordial perturbations from a source such as inflation and from topological defects to have a different anisotropy power spectra particularly in the region of the "Doppler" peaks [1]. The angular resolution and sensitivity of Planck will allow discrimination between these alternatives with tests of both the power spectrum and statistics.

The high-order multipoles will allow an accurate measure of the spectral index n of the primordial fluctuation spectrum:

$$(\delta\phi)^2 \propto \lambda^{(1-n)} \tag{1}$$

where $\delta\phi$ is the potential fluctuation responsible for the CBR anisotropies, and λ is the scale of the density perturbation. This corresponds to CBR temperature fluctuations $(\Delta T/T)^2 \propto \theta^{(1-n)}$ for angles $\theta > 30' \ \Omega_0^{1/2}$. The proposed observations will be able to verify accurately the nearly scale invariant "Harrison–Zel'dovich" spectrum ($n = 1$) predicted by inflation. Any significant deviation from that value would have extremely important consequences for the inflationary paradigm. The COBE–DMR limit on the spectral index after four years of observations ($n = 1.1^{+0.2}_{-0.3}$, 68% CL; [30]) can be constrained ~ 10 times better by the Planck results.

The proposed observations will provide an additional, independent test for the inflationary model. Temperature anisotropies on large angular scales can be generated by gravitational waves (tensor modes, T), in addition to the energy-density perturbation component (scalar modes, S). Most inflationary models predict a well determined, simple relation between the ratio of these two components, T/S, and the spectral index n [21], [51]:

$$n \approx 1 - \frac{1}{7}\,\frac{T}{S}. \tag{2}$$

The Planck maps maybe able to verify this relationship, since the temperature anisotropies from scalar and tensor modes vary with multipoles in different ways.

A good satellite mission will be able not only to test the inflationary concept but also to distinguish between various models and determine inflationary parameters. There is an extensive literature on what can be determined about inflation such as the scalar and tensor power spectra, the energy scale of inflation and so on (see e.g. [73], [40]). Such quality measurements lead also to good observations or constraints for Ω_0, Ω_{baryon}, Λ, H_0, etc. Sub–degree anisotropies are sensitive to the ionization history of the universe. In fact, they can be erased if the intergalactic medium underwent reionization at high redshifts. Moreover, the temperature anisotropies at small angular scales depend on other key cosmological parameters, such as the initial spectrum of irregularities, the baryon density of the universe, the nature of dark matter, and the geometry of the universe (see e.g. [20], [39], [36], [68]. The Planck maps will provide constraints on these parameters within the context of specific theoretical models.

Moreover, Planck should measure the Sunyaev–Zel'dovich effect for more than 1000 rich clusters, using the higher resolution bolometric channels. This will allow a rich analysis of clusters. Combined with X–ray observations these measurements can be used to estimate the Hubble constant H_0 as a second independent determination.

8.2.3. *Foreground Emissions*

In order to obtain these scientific goals, the measured temperature fluctuations need to be well understood in terms of the various components that add to the cosmological signal. In fact, in addition to the CBR temperature fluctuations, foreground structures will be present from weak, unresolved extragalactic sources and from radiation of Galactic origin (interstellar dust, free–free and synchrotron radiation).The Planck observations will reach the required control on the foreground components in two ways. First, the large sky coverage ($\geq 90\%$ of the sky) will allow accurate modeling of these components where they are dominant (e.g. Galactic radiation near the galactic plane). Second, the observations will be performed in a very broad spectral range.

The Planck channels will span the spectral region of minimum foreground intensity (in the range 50–300 GHz), but with enough margin at high and low frequency to monitor "in real–time" the effect of the various foreground components (see e.g. Brandt et al. 1994). By using the Planck spectral information and modeling the spectral dependence of galactic and extragalactic emissions it will be possible to remove the foreground contributions with high accuracy.

It should be noted that in most channels the ultimate limitation to the cosmological information of high-quality CMB maps is expected to be due to the residual uncertainties in the separation of the foreground components rather than statistical noise. This explains why the overall design of Planck is highly driven by the need of achieving as large a spectral coverage as possible. Making the observations where the dominant foreground components are different will permit a powerful cross check on residual systematic errors in the CBR temperature fluctuation maps.

The Phase A Study provides a baseline design for the mission, spacecraft, and instruments. Broad frequency coverage is achieved with arrays of HEMT amplifiers (30–100 GHz) and bolometers (100–850 GHz). The amplifiers use GaAs MMICs (monolithic microwave integrated circuits) cooled passively to about 100 K. At the end of the Phase A study the number of detectors and focal plane layout were optimized for the passively cooled LFI configuration. This is summarized in Table 8.2.3

During the time since the Phase A study work has continued and it has been learned that converting to InP HEMT amplifiers and actively cooling

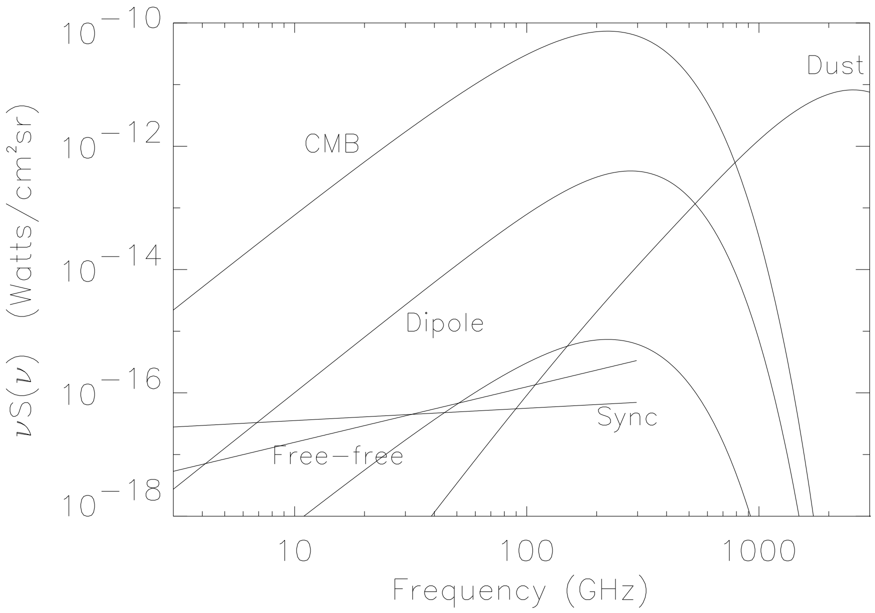

Figure 13. The intensity of the microwave sky from 3 to 3000 GHz near a Galactic latitude of $b = 20°$. The ordinate is the brightness of the sky times the frequency. which means the plot indicates the distribution of power per unit bandwidth. For synchrotron emission $S(\nu) \propto \nu^{-0.7}$; for free-free emission $S(\nu) \propto \nu^{-0.1}$; and for dust emission near 100 GHz $S(\nu) \propto \nu^{3.7}$. The scaling in effective temperature is $T(\nu) \propto \nu^{-2} S(\nu)$. The lowest Planck-like curve is for T = 27 μK or anisotropy at the 10^{-5} level.

to 20 K provides an inprovement in performance and that changing some operating parameters the instrument might be improved in other ways. Table 8.2.3 shows another possible configuration taking advantage of the developments since the end of Phase A.

The need of accurate characterization of all non-cosmological components, of course, brings the benefit of additional astrophysical information. The very large Planck data base, particularly when combined with the IRAS survey, can provide information on several non–cosmological issues, such as the evolution of starburst galaxies, the distribution of a cold–dust component, or the study of low–mass star formation.

8.2.4. *The Payload*

The Planck model payload consists mainly of a shielded, off-axis Gregorian telescope, with a parabolic primary reflector and a secondary mirror, leading to an integrated instrument focal plane assembly. The payload is part of a spinning spacecraft, with a spin rate of 1 rpm. The focal plane

1st Phase A Planck Payload Characteristics								
Telescope	1.5 m Diam. Gregorian; system emissivity $\leq$1% Viewing direction offset $\geq 70°$ from spin axis							
Instrument	LFI				HFI			
Center Frequency (GHz)	31.5	53	90	125	140	222	400	714
Wavelength (mm)	9.5	5.7	3.3	2.4	2.1	1.4	0.75	0.42
Bandwidth ($\frac{\Delta\nu}{\nu}$)	0.15	0.15	0.15	0.15	0.4	0.5	0.7	0.6
Detector Technology	HEMT receiver arrays				Bolometers arrays			
Detector Temperature	$\sim$ 100 K				0.1 - 0.15 K			
Cooling Requirements	Passive				Cryocooler + Dilution system			
Number of Detectors	13	13	13	13	8	11	16	16
Angular Resolution (arcmin)	30	20	15	12	10.5	7.5	4.5	3
Optical Efficiency	1	1	1	1	0.3	0.3	0.3	0.3
$\frac{\Delta T}{T}$ Sensitivity ($1\sigma, 10^{-6}$ units, 90% sky coverage, 2 years)	1.7	2.7	4.1	7.2	0.9	1.0	8.2	10^4
$\frac{\Delta T}{T}$ Sensitivity ($1\sigma, 10^{-6}$ units, 2 % sky coverage, 2 years)	0.6	0.9	1.4	2.4	0.3	0.3	2.7	5000

TABLE 6. Instrumental Parameters for Planck the most important factors are the frequency coverage, the angular resolution, sky coverage, and sensitivity.

assembly is divided into low-frequency (LFI) and high-frequency (HFI) instrumentation according to the technology of the detectors. Both the LFI and the HFI are designed to produce high-sensitivity, multifrequency measurements of the diffuse sky radiation. The LFI will measure in four bands in the frequency range 30–130 GHz (2.3–10 mm wavelength). The HFI will measure in four channels in the range 140–800 GHz (0.4–2.1 mm wavelength). The highest frequency LFI channel and the lowest HFI channel overlap near the minimum foreground region. Both the HFI and LFI teams are reinvestigating the optimal frequency bands. Table 6 summarizes the main characteristics of the Planck payload.

8.2.5. *The Main Optical System*

A clear field of view is necessary for the optics of a high-sensitivity CMB anisotropy experiment to avoid spurious signals arising from the mirrors or

Final PHASE A INSTRUMENT SUMMARY

Characteristic	LFI				HFI				
Detector technology	HEMT arrays				Bolometer arrays				
Detector temperature	~ 100 K				0.1–0.15 K				
Center frequency [GHz]	31.5	53	90	125	143	217	353	545	857
Number of detectors	4	14	26	12	8	12	12	12	12
Angular resolution [$'$]	30	18	12	12	10.3	7.1	4.4	4.4	4.4
Bandwidth [$\Delta\nu/\nu$]	0.15	0.15	0.15	0.15	0.37	0.37	0.37	0.37	0.37
Noise/res. element, in 15 months [μK]	21	20	39	97	3.3	5.5	33	210	11,000

TABLE 7. Proposed "conservative" Planck (COBRAS/SAMBA) instrument configuration at the end of the Phase A study. It was based upon MMIC GaAs and early micromesh bolometer technology and a mix of cryocooler options.

POTENTIAL PLANCK INSTRUMENT SUMMARY

Characteristic	LFI				HFI					
Detector technology	HEMT arrays				Bolometer arrays					
Detector temperature	20 K				0.1–0.15 K					
Center frequency [GHz]	30	44	70	100	100	143	217	353	545	857
Number of detectors	4	6	10	30	4	12	12	6	6	6
Angular resolution [$'$]	34	23	16	10	14	10	7.1	4.4	4.4	4.4
Bandwidth [$\Delta\nu/\nu$]	0.20	0.20	0.20	0.20	0.25	0.25	0.25	0.25	0.25	0.25
Noise/res. element, in 15 months [μK]	5	7	10	17	3	4	7	41	240	10,600
Both polarizations?	yes	yes	yes	yes	no?	yes	yes	no?	no	no

TABLE 8. Potential Planck detector configuration based upon active LFI cooling, InP HEMT amplifiers, more advanced micromesh, filter, feedhorn, and polarizer technology.

from supports and mechanical mounting. The off-axis Gregorian configuration has a primary parabolic mirror of 1.5 meter, and an elliptic secondary mirror (0.57 m diameter). Stray satellite radiation and other off–axis emissions are minimized by underilluminating the low–emissivity optics. The telescope reimages the sky onto the focal plane instrument located near the payload platform. The telescope optical axis is offset by 70° to 90° from the spin axis. Thus at each spacecraft spin rotation the telescope pointing direction sweeps a large (approaching a great) circle in the sky, according to the sky scan strategy.

Blockage is a particularly important factor since several feeds and de-

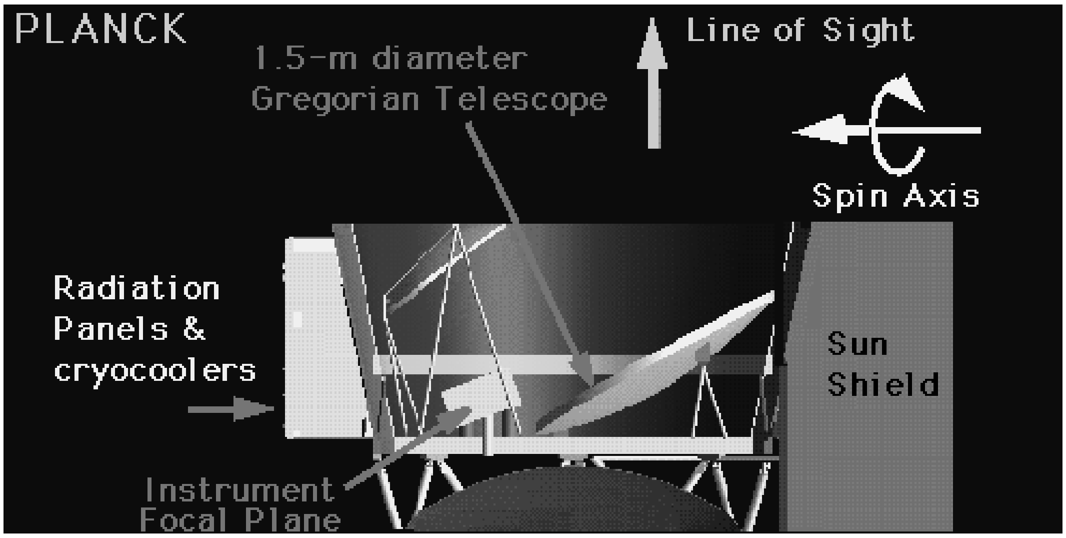

Figure 14. Artist's concept of one possible configuration of the Planck Surveyor optics and focal plane layout.

tectors are located in the focal plane, and unwanted, local radiation (e.g. from the Earth, the Sun and the Moon) needs to be efficiently rejected. A large, flared shield surrounds the entire telescope and focal plane assembly, to screen the detectors from contaminating sources of radiation. The shield also plays an important role as an element of the passive thermal control of the spacecraft.

8.2.6. *The Focal Plane Assembly*

The necessary wide spectral range requires the use of two different technologies, bolometers and coherent receivers incorporated in a single instrument. Both technologies have shown impressive progress in the last ten years or so, and more is expected in the near future. The thermal requirements of the two types of detectors are widely different. The coherent radiometers (LFI), operating in the low frequency channels, give good performance at and operational temperature of $\sim$ 100 K, which is achievable with passive cooling. Splitting the HEMT chain into cool and warmer portions leads to a passive cooling temperature of 65 K and with active cooling 20 K. The bolometers, on the other hand, require temperatures $\leq$ 0.15 K in order to reach their extraordinary sensitivity performances. The main characteristics of the LFI and HFI are summarized in Table 6.

The LFI consists of an array of 26 corrugated, conical horns, each exploited in the two orthogonal polarization modes, feeding a set of state–of–the–art, high sensitivity receivers. The receivers will be based on MMIC

(Monolithic Microwave Integrated Circuits) technology with HEMT (High Electron Mobility Transistor) ultra–low noise amplifiers (see e.g. Pospieszalski et al. 1993). Since the whole LFI system will be passively cooled, it can be operated for a duration limited only by spacecraft consumables (up to 5 years). If actively cooled with a sorption cooler, it can still operate for 5 years as there is no significant cryogen depeletion; however, the HEMT chain must be broken into two sections. The three lowest center frequencies of the LFI were chosen to match the COBE-DMR channels, to facilitate the comparison of the product maps. The exact frequency bands are being reviewed in the upgraded design.

About 50 bolometers will be used in the HFI instrument, which require cooling at ~ 0.1 K. The cooling system combines active coolers reaching 4 K with a dilution refrigeration system working at zero gravity. The refrigeration system will include two pressurized tanks of ^{3}He and ^{4}He for an operational lifetime of 2 years.

8.2.7. *Orbit and Sky Observation Strategy*

One of the main requirements for the Planck mission is the need of a far–Earth orbit. This choice greatly reduces the problem of unwanted radiation from the Earth which is a serious potential contaminant at the high goal sensitivity and angular resolution. The requirements on residual Earth radiation are basically the same for the LFI and the HFI systems. Adopting a low–earth orbit, such as that used by the COBE satellite, the requirement on straylight and sidelobe rejection would be a factor of 10^{13}, which is beyond the capabilities of present microwave and sub–mm systems and test equipment. Two orbits have been considered for Planck: a small orbit around the L5 Lagrangian point of the Earth–Moon system, at a distance of about 400,000 km from both the Earth and the Moon and the L2 Lagrange point of the Earth–Sun system. From the Earth–Moon Lagrange point the required rejection is relaxed by four orders of magnitude, which is achievable with careful, standard optical designs. For the Earth–Sun L2 point the situation for the Earth and Moon is even better and the Sun is basically unchanged but because the Earth, Moon, and Sun are all roughly in the same direction, the spacecraft can be oriented very favorably.

These orbits are also very favorable from the point of view of passive cooling and thermal stability [26]. The spacecraft will be normally operated in the anti-solar direction, with part of the sky observations performed within $\pm 40°$ from anti–solar.

Other potential missions considered both a heliocentric orbit and the Earth–Sun L2 point. All concerned seemed to have come to the conclusion that the Earth–Sun L2 point is the best choice. Operationally, it is difficult to find a more optimum location.

The main goal of the mission is to observe nearly the whole sky ($\gtrsim 90\%$) with a sensitivity of 10–15 μK within the two year mission lifetime. Deeper observation of a limited ($\sim$ 2%) sky region with low foregrounds could significantly contribute to the cosmological information. Simulations have shown that these observational objectives can be achieved simultaneously in a natural way, using the spinning and orbit motion of the spacecraft, with relatively simple schemes.

9. Interpretation & Future

In five short years the field of CMB anisotropy observations and theory has made great strides. Until April 1992 all plots of CMB anisotropy showed only upper limits, except for the $\ell = 1$ dipole. Now we are beginning to trace out the shape of the power spectrum and to make maps of the anisotropies. This observational program promises to deliver a wealth of new information to cosmology and to connect it to other fields. The COBE DMR has now released the full four-year data set. We can expect little in the way of improvement compared to the final DMR results from future experiments on the large angular scales but scientific interest has moved to covering the full spectrum and learning what the medium and small angular scales will tell us. Already we are seeing plots showing the CMB anisotropy spectrum related to and overlaid on the primordial density perturbation power spectrum and attempts to reconstruct the inflaton potential. These are the first steps in a new period of growth.

The last table gives an example of the level of sensitivity that might be achieved by the many experiments are underway, planned, and approved. Nearly every group has data under analysis and is also at work on developing new experiments. Some of these are the natural extensions of the ongoing experiments. Some groups are considering novel approaches. Real long-term progress depends on avoiding the potential foregrounds: fluctuations of the atmosphere, a source of noise that largely overwhelms recent advances in detector technology, and Galactic and extragalactic signals. This requires instruments having sufficient information (usually only through multifrequency observations) and observing frequencies to separate out the various components. It also means going above the varying atmosphere. Collaborations are working on long-duration ballooning instruments. Ultimately, as COBE has shown, going to space really allows one to overcome the atmospheric problem and to get data in a very stable and shielded environment. The two selected satellite mission are actively being developed. We can anticipate a steady and significant advance in observations. With the new data that are appearing, can be expected, and ultimately will come from the Planck mission we can look forward to a very significant improve-

	1997	BOOM/MAX	MAP*	Planck*
Ω	0.01 - 2	6%	18%	1%
Ω_b	$0.01h^{-2}$	30%	10%	0.7%
$\Lambda(\Omega_\Lambda)$	< 0.65	±0.10	±0.43	±0.05
Ω_ν	< 2	±0.25	±0.08	±0.03
t_0	12-18 Gyr	—	—	—
H_0	30-80 km/s/Mpc	10%	20%	2%
σ_8	0.5-0.6	30%	30%	10%
Q	$20 \pm 2\ \mu$K*	"	"	"
n_s	1.0 ± 0.5	30%	5%	1%
τ	0.01 - 1	±0.5	±0.2	±0.15
T_0	2.73 ± 0.01*	—	—	—
Y	0.2-0.25	10%	10%	7%
T/S	0.0 - 1	±1.6	±0.38	±0.09

TABLE 9. Projected Parameter Errors: Assumes variation around Standard CDM. (*Bond et al., 1997.) Note that parameters are not all independent, e.g., $H_0 t_0 = f(\Omega, \Lambda)$.

ment in our knowledge of cosmology.

Acknowledgements

This work was supported in part by the Director, Office of Energy Research, Office of High Energy and Nuclear Physics, Division of High Energy Physics of he U.S. Department of Energy under contract No. DE-AC03-76SF00098.

References

1. Albrecht, A., Coulsen, D., Ferreira, P., & Magueijo, J., 1995 Phys. Rev. Lett. 76, 1413. astro-ph 9505030.
2. Alsop, D. C., et al. 1992, ApJ, 395, 317
3. Alpher, R.A. & R.C. Herman 1948 Physics Today, Vol. 41, No. 8, p. 24
4. Banday, A. et al. 1996a, ApJ, 468, L85. astro-ph/9601064
5. Banday, A. et al. 1996b, ApJ, 464, L1, astro-ph/9601066
6. Bennett, C. L., et al. 1996, ApJ, 464, L1, astro-ph/9601067
7. Bennett, C. L., et al. 1994, ApJ, 436, 423
8. Bennett, C. L., et al. 1993, ApJ, 414, L77
9. Bennett, C. L., et al. 1992, ApJ, 396, L7
10. Bennett, C. L., et al. 1991, ApJ, 391, 466
11. Bock, J. et al. Proceedings of "Submillimeter and Far-Infrared Space Instrumentation," 30^{th} ESLAB Symposium, 24-26 Sept. 1996, ESTEC, Noordwijk, The Netherlands.
12. J.R. Bond astrop-ph/9407044 (1994)
13. Brandt, W.N., Lawrence, C.R., Readhead, ACS, Pakianathan, & Fiola, T.M., 1993

accepted Ap.J.
14. Clapp, A. C., Devlin, M. J., Gundersen, J. O., Hagmann, C. A., Hristov, V. V., Lange, A. E., Lim, M., Lubin, P. M., Mauskopf, P. D., Meinhold, P. R., Richards, P. L., Smoot, G. F., Tanaka, S. T., Timbie, P. T. & Wuensche, C. A. 1994, ApJL, 433, 57-60. astro-ph/9404072
15. Cheng, E. S., Cottingham, D. A., Fixsen, D. J., Inman, C. A., Kowitt, M. S., Meyer, S. S., Page, L. A., Puchalla, J. L., Ruhl, J. & Silverberg, R. F. 1996, ApJ, 456, L71 astro-ph/9508087.
16. Clapp, A. C., Devlin, M. J., Gundersen, J. O., Hagmann, C. A., Hristov, V. V., Lange, A. E., Lim, M., Lubin, P. M., Mauskopf, P. D., Meinhold, P. R., Richards, P. L., Smoot, G. F., Tanaka, S. T., Timbie, P. T. & Wuensche, C. A. 1994, ApJL, 433:57-60 astro-ph/9404072
17. Cayon, L., & Smoot, G.F., 1995 Astrophysical Journal, 452:487 astro-ph/9504072.
18. Costa, A. de Oliveira-, & Smoot, G.F., 1995, Astrophysical Journal, 448:477. astro-ph/9412003
19. Coulson, D., Ferreira, P., Graham, P., & Turok, N., 1994, Nature, 368, 27
20. Crittenden, R., Bond, J.R., Davis, R.L., Efstathiou, G., & Steinhardt, P., 1993, Phys. Rev. Lett., 71, 324
21. Davis, R.L., Hodges, H.M., Smoot, G.F., Steinhardt, P.J., Turner, M.S.; 1992, PRL, 69, 1856. erratum 70:1733
22. Devlin, M. J., Clapp, A. C., Gundersen, J. O., Hagmann, C. A., Hristov, V. V., Lange, A. E., Lim, M., Lubin, P. M., Mauskopf, P. D., Meinhold, P. R., Richards, P. L., Smoot, G. F., Tanaka, S. T., Timbie, P. T. & Wuensche, C. A. 1994, ApJL, **430**, L1. astro-ph/940403
23. R.H. Dicke, P.J.E. Peebles, P.G. Roll, and D.T. Wilkinson1965 Ap.J. 142, 414.
24. A.G. Doroshkevich, V.N. Lukash & I.D. Novikov 1973 The Isotropization of Homogeneous Cosmological Models *Zh. Eksper. Teor. Fiz* **64**, 739–746.
25. A.G. Doroshkevich, V.N. Lukash & I.D. Novikov 1974 Primordial Radiation in a Homogeneous but Anisotropic Universe *Astron. Zh.* **51**, 554–560.
26. Farquhar, R.W & Dunham D.W., 1990; *Observatories in Earth Orbit & Bejond*, Y.Kondo Ed., Kluwer, p.391.
27. Fischer, M. L., et al. 1992, ApJ, 388, 242
28. Fixsen, D. J., et al. 1996, ApJ, accepted, astro-ph/9605054
29. Ganga, K., et al. 1993, ApJ, 410, L57
30. Górski K.M. et al., 1996, ApJ, 464, L11. astro-ph/9601063
31. Harrison, E. R. 1970, Phys. Rev. D, 1, 2726
32. Hauser, M. G. & Peebles, P. J. E. 1973, ApJ, 185, 757
33. Hinshaw, G., et al. 1996a, ApJ Letters, 464, L17. astro-ph/9601058
34. Hinshaw, G., et al. 1996b, ApJ Letters, 464, L25. astro-ph/9601061
35. Hobson M.P., Lasenby A.N. & Jones M., 1995, MNRAS submitted.
36. Hu, W., Scott, D., & Silk, J., 1994, ApJ., 430, L5
37. Hu, W., D. Spergel, & M. White 1996 PRD 55, 3288 astro-ph/9605193
38. Jungman, G., Kamionkowski, M., Kosowsky, A., & Spergel, D. N. 1995, PRL 76, 1007. astro-ph/9512139
39. M. Kamionkowski, D.N. Spergel, & N. Sugyiama 1994 ApJ 426, L1.
40. Knox, L. 1995, Phys. Rev. **D** 1995 52, 4307. astro-ph/9504054
41. Kogut, A., et al. 1992, ApJ, 401, 1
42. Kogut, A., Banday, A. J., Bennett, C. L., Hinshaw, G., Loewenstein, K., Lubin, P., Smoot, G. F., & Wright, E. L. 1994, ApJ, 433, 435
43. Kogut, A., et al. 1996a, ApJ, 460, 1. astro-ph/9601066
44. Kogut, A., et al. 1996b, ApJ, 464, L5. astro-ph/9601060
45. Kogut, A., et al. 1996c, ApJ, 464, L29. astro-ph/9601062
46. Lee, A. T. et al. 1996, Preprint, To appear in Appl. Phys. Lett.
47. M. A. Lim, A. C. Clapp, M. J. Devlin, N. Figueiredo, J. O. Gundersen, S. Hanany, V. V. Hristov, A. E. Lange, P. M. Lubin, P. R. Meinhold, P. L. Richards, J. W. Staren,

G. F. Smoot, S. T. Tanaka astro-ph/9605142
48. Lineweaver, C., et al. 1994 Ap. J., 436, 452. (astro-ph/9403021)
49. Lineweaver, C., et al. 1995, ApJ, 448, 482-487.
50. Lineweaver, C., et al. 1996, ApJ, 470, 38. astro-ph/9601151
51. Little & Lyth 1992 PLB, 291, 391.
52. N. Mandolesi, G.F. Smoot, M. Bersanelli, C. Cesarsky, M. Lachieze-Rey, L. Danese, N. Vittorio, P. De Bernardis, G. Dall'Oglio, G. Sironi, P. Crane, M. Janssen, B. Partridge, J. Beckman, R. Rebolo, J. L. Puget, E. Bussoletti, G. Raffelt, R. Davies, P. Encrenaz, V. Natale, G. Tofani, P. Merluzzi, L. Toffolatti, R. Scaramella, E. Martinez-Gonzales, D. Saez, A. Lasenby, G. Efstathiou; 1993, *COBRAS*, proposal submitted to ESA M3.
53. Mandolesi, N., Bersanelli, M., Cesarsky, C., Danese, L., Efstathiou, g, Griffin, M., Lamarre, J.M., Norgaard-Nielson, H.U., Pace, O., Puget, J.L., Raisanen, A., Smoot, G.F., Tauber, J., & Volonte, S. 1995, Planetary & Space Sciences 43, 1459.
54. Mather, J. C., et al. 1994, ApJ, 420, 439
55. Meinhold, P., et al. 1993, ApJ, 409, L1
56. O'Sullivan C. et al., 1995, MNRAS, submitted.
57. Ganga, K, Page, L. Cheng, E., Meyer, S. 1994 astro-ph/9404009
58. L. Page 1997 astro-ph/9703054
59. Peebles, P. J. E. 1973, ApJ, 185, 413
60. Peebles, P. J. E. & Yu, J. T. 1970, ApJ, 162, 815
61. P.J.E. Peebles, 1993, "Principles of Physical Cosmology," Princeton U. Press, p. 168
62. A.A. Penzias and R. Wilson 1965, Ap. J. 142, 419.
63. Puget, J.L., Ade, P., Benoit, A., De Bernardis, P., Bouchet, F., Cesarsky, C., Desert, F.X., Gispert, R., Griffin, M., Lachieze–Rey, M., Lamarre, J.M., De Marcillac, P., Masi, S., Melchiorri, F., Pajot, F., Rowan–Robinson, M., Serra, G., Torre, J.P., Vigroux, L., White, S.; 1993, *SAMBA*, proposal submitted to ESA M3.
64. Robson M., Yassin G., Woan G., Wilson D.M.A., Scott P.F., Lasenby A.N., Kenderdine S., Duffett-Smith P.J., 1993 A&A, 277, 314.
65. Robson M., O'Sullivan C.M.M., Scott P.F., Duffett-Smith P.J., 1994, A&A, 286, 1028.
66. Robson M., 1994, PhD thesis, (University of Cambridge).
67. R. K. Sachs & A.M. Wolfe 1967, Ap.J. 147, 73.
68. D. Scott. J. Silk, and M. White 1995, Science, 268, 829
69. J. Silk 1967, Nature, 215, 1155-1156.
70. Smoot, G.F., et al. 1990, ApJ, 360, 685
71. Smoot, G. F., et al. 1992, ApJ, 396, L1
72. Smoot, G. F., Tenorio, L., Banday, A.J., Kogut, A., Wright, E.L., Hinshaw, G., & Bennett, C.L. 1994, ApJ, 437, 1
73. Steinhardt, P.J., 1995, Proc. of Snowmass Workshop,
74. S. T. Tanaka, A. C. Clapp, M. J. Devlin, N. Figueiredo, J. O. Gundersen, S. Hanany, V. V. Hristov, A. E. Lange, M. A. Lim, P. M. Lubin, P. R. Meinhold, P. L. Richards, G. F. Smoot, J. Staren 1996, ApJ 468, L81 astro-ph/9512067
75. S. T. Tanaka, et al. in prep.
76. Tegmark, M. & Bunn, E. F. 1995, ApJ, 455, 1
77. M. Tegmark, A. N. Taylor, & A.F. Heavens astro-ph/9603021 (1996)
78. M. Tegmark, A. de Oliveira-Costa, D.J. Devlin, C.B. Netterfield, L. Page & E.J. Wollack astro-ph/9608019 (1996)
79. White, M. & E.F. Bunn 1995, ApJ 443, L53 astro-ph/9510088
80. M. White, D. Scott, and J. Silk, Ann. Rev. Astron. & Astrophys. **32**, 329 (1994)
81. White, M. 1996, Phys Rev D, 53, 3011 astro-ph/9601158
82. Wright, E. L., et al. 1992, ApJ, 396, L13
83. Wright, E. L., et al. 1996, ApJ Letters, 464, L21. astro-ph/9601059
84. Wright, E. L., F. Hinshaw & C.L. Bennett 1996, ApJ, 458, L53
85. Zeldovich, Ya B. 1972, MNRAS, 160, 1

CMB Anisotropy Experiment References

86. ACE and BEAST. These two new projects are aimed at using HEMTs between 26 and 100 GHz on both super-pressure and conventional long-duration balloon platforms. The finest angular resolution will be near $1/5°$.
87. APACHE. This experiment will observe from Dome-C in the Antarctic. Web site http://tonno.tesre.bo.cnr.it/ valenzia/APACHE/apache.html contains more information.
88. ARGO. A balloon-borne bolometer based experiment. Results are reported in de Bernardis, et al. 1994, Ap.J. 422:L33.
89. ATCA: Australia Telescope Compact Array. An interferometer operating at 8.7 GHz with a 2' resolution produced a map that was analyzed for anisotropy. The results are reported in Subrahmanyan R., Ekers, R. D., Sinclair, M. & Silk, J. 1993, MNRAS 263:416.
90. BAM: Balloon Anisotropy Measurement. This uses a differential Fourier transform spectrometer to measure the spectrum of the anisotropy between 90 and 300 GHz. Recent results are reported in astro-ph/9609108. More information may be obtained from http:/cmbr.physics.ubc.edu.
91. Bartol. This is a bolometer-based experiment designed to look at $2°$ angular scales. It observed from the Canary Islands. Results are reported in Piccirillo et al., astro-ph/9609186.
92. BOOMERanG is a collaboration between the Caltech, Berkeley, Santa Barbara (Ruhl) and Rome groups. It will use bolometers to measure the anisotropy in the CMB between 90 and 410 GHz. The ultimate goal is a circumpolar Antarctic flight.
93. CBI: Cosmic Background Imager. This is an interferometer that plans to produce maps of the microwave sky near 30 GHz.
94. HACME/SP. This uses HEMTs on the ACME telescope. Observations were made from the South Pole. Recent results are reported in Gundersen, J. et al. 1995, Ap.J. 443:L57.
95. IAB. A bolometer-based experiment carried out at spectrum of the anisotropy between 90 and 300 GHz. Recent results are reported in astro-ph/9609108. More information may be obtained from http://cmbr.physics.ubc.edu.
96. Bartol. This is a bolometer-based experiment designed to look at $2°$ angular scales. It observed from the Canary Islands. Results are reported in Piccirillo et al., astro-ph/9609186.
97. BOOMERanG is a collaboration between the Caltech, Berkeley, Santa Barbara (Ruhl) and Rome groups. It will use bolometers to measure the anisotropy in the CMB between 90 and 410 GHz. The ultimate goal is a circumpolar Antarctic flight.
98. CAT. This is the Cambridge Anisotropy Telescope. It operates near 15 GHz and produces images of the microwave background. Early results are reported in Scott et al. 1996, Ap.J. 461:L1.
99. CBI: Cosmic Background Imager. This is an interferometer that plans to produce maps of the microwave sky near 30 GHz.
100. *COBE* is the COsmic Background Explorer. The three experiments aboard the satellite are the Differential Microwave Radiometers (30-90 GHz, DMR), the Far-InfraRed Absolute Spectrophotometer (60-630 GHz, FIRAS), and the Diffuse InfraRed Background Experiment (1.2-240 μm, DIRBE) All the experiments produce maps of the sky.
101. FIRS. The Far InfraRed Survey. This is an experiment that started at MIT but has since moved to Princeton, University of Chicago and NASA/GSFC. It is a bolometer-based balloon-borne radiometer. It confirmed the initial *COBE*/DMR discovery.
102. HACME/SP. This uses HEMTs on the ACME telescope. Observations were made from the South Pole. Recent results are reported in Gundersen, J. et al. 1995, Ap.J. 443:L57.
103. IAB. A bolometer-based experiment carried out at the Italian Antarctic Base. Results are reported in Piccirillo, L. & Calisse, P. 1993, Ap.J. 413:529.

104. MAT. This is the Mobile Anisotropy Telescope. It is similar to QMAP but is designed to operate from the ground in Chile.
105. MAX was a collaboration between UCSB and Berkeley. It is a balloon-borne bolometer-based radiometer spanning roughly between 90 and 420 GHz. Recent results are reported in Lim et al. 1996, Ap. J. 469:L69. It flew on the ACME telescope.
106. MAXIMA is a collaboration between Berkeley, Italy, and CalTech. It is the next generation of MAX. Web site http://physics7.berkeley.edu/group/cmb/gen.html contains more information.
107. MSAM. There are a number of versions of MSAM. All use bolometers of various sorts and fly on balloons. The MSAM collaboration includes NASA/GSFC, Bartol Research Institute, Brown University, and the University of Chicago.
108. OVRO. The Owen's Valley Radio Observatoty telescopes operate with various receivers between 15 and 30 GHz. The 40 m dish has a $2'$ beam, and the 5.5 m has a $7.3'$ beam. The experiments are aimed primarily at small angular scales.
109. PYTHON. A multi-pixel bolometer- and HEMT- based experiment operated from the ground at the South Pole. The experiment has run in a number of configurations. Recent results are reported in Ruhl, J., et al. 1995, Ap.J., 453:L1.
110. QMAP. This is a balloon-borne experiment that uses a combination of HEMTs and SIS detectors. The angular resolution is $1/5°$. This experiment is designed to produce "true" maps of the sky.
111. SASK. These experiments are based on HEMT amplifiers operating between 26 and 46 GHz. They were performed in Saskatoon, Saskatchewan CA. Three years of observations have gone into the final data set.
112. SuZIE is a bolometer-based experiment that observes from the ground. It is primarily intended to measure the SZ effect at high frequencies though it will also give information on the anisotropy at small scales.
113. TopHat is a collaboration between Bartol Research Institute, Brown University, DSRI, NASA/GSFC, and the University of Chicago. The group plans to observe with an extremely light-weight bolometer-based payload mounted on top of a scientific balloon that circumnavigates the Antarctic. For more information see http://cobi.gsfc.nasa.gov/msam-tophat.html.
114. Tenerife. Ground-based differential radiometers with 10-33 GHz receivers. The resolution is about $6°$. The experiment observes from the Observatorio del Teide in Tenerife, Spain. It has operated for many years. Recent results are discussed in Hancock et al. 1994, Nature, 367, 333.
115. VCA: Very Compact Array. This is an interferometer being developed at the University of Chicago. It will produce maps of the CMB at 30 GHz and be sensitive to larger angular scales than CBI.
116. VLA. This is work done near 5 GHz, on arcminute and smaller angular scales. It uses the Very Large Array. Recent results are reported in Fomalont et al. 1993, Ap.J. 404:8-20.
117. VSA: Very Small Array. This is a 30 GHz interferometer; the next generation of CAT. Web site http://www.mrao.com.ac.uk/telescopes/cat/vsa.html contains more information.
118. White Dish. This experiment uses and on-axis Cassegrain telescope and a 90 GHz single-mode bolometer. It observed at the South Pole and is sensitive to small angular scales. Results are reported in Tucker et al., 1993, Ap.J. 419:L45.